Human iPSC-derived neural progenitors are an effective drug discovery model for neurological mtDNA disorders

Lorenz, C., Lesimple, P., Bukowiecki, R., Zink, A., Inak, G., Mlody, B., Singh, M., Semtner, M., Mah, N., Auré, K., Leong, M., Zabiegalov, O., Lyras, E.M., Pfiffer, V., Fauler, B., Eichhorst, J., Wiesner, B., Huebner, N., Priller, J., Mielke, T., Meierhofer, D., Izsvák, Z., Meier, J.C., Bouillaud, F., Adjaye, J., Schuelke, M., Wanker, E.E., Lombès, A., Prigione, A.

This is the final version of the accepted manuscript. The original article has been published in final edited form in:

Cell Stem Cell
2017 MAY 04 ; 20(5): 659-674.e9
2017 JAN 26 (first published online)
doi: 10.1016/j.stem.2016.12.013

Publisher: Cell Press / Elsevier

Human iPSC-derived neuronal progenitors are an effective drug discovery model for neurological mitochondrial DNA disorders

Authors and affiliations:

Carmen Lorenz[1,2*], Pierre Lesimple[3,4,5*], Raul Bukowiecki[1], Annika Zink[1,6], Gizem Inak[1], Barbara Mlody[1], Manvendra Singh[1], Marcus Semtner[1], Nancy Mah[6], Karine Auré[3,4,5], Megan Leong[1], Oleksandr Zabiegalov[1], Ekaterini-Maria Lyras[6], Vanessa Pfiffer[1], Beatrix Fauler[7], Jenny Eichhorst[9], Burkhard Wiesner[9], Norbert Huebner[1], Josef Priller[2,6,8], Thorsten Mielke[7], David Meierhofer[7], Zsuzsanna Izsvák[1], Jochen C. Meier[1,10], Frédéric Bouillaud[3,4,5], James Adjaye[11], Markus Schuelke[6], Erich E. Wanker[1], Anne Lombès[3,4,5§], Alessandro Prigione[1§]

[1]Max Delbrueck Center for Molecular Medicine (MDC), Berlin, Germany

[2]Berlin Institute of Health (BIH), Berlin, Germany

[3]INSERM U1016, Institut Cochin, Paris, France

[4]CNRS UMR 8104, Paris, France

[5]Université Paris Descartes, France

[6]Charité – Universitätsmedizin, Berlin, Germany

[7]Max Planck Institute for Molecular Genetics, Berlin, Germany

[8]DZNE, Berlin, Germany

[9]Leibniz Institut für Molekulare Pharmakologie (FMP), Berlin, Germany

[10]Zoological Institute, Braunschweig, Germany

[11]Institute for stem cell research and regenerative medicine, Medical Faculty, Heinrich Heine University, Duesseldorf, Germany

*Equal contribution

Running Title: iPSC-derived NPCs for treatment discovery of mtDNA disease

[§]**Contact information**:

Alessandro Prigione, M.D. Ph.D. Robert-Roessle-Str. 10, D-13125 Berlin-Buch, Germany. Phone: 0049-30-9406-2871, Fax: 0049-30-9406-3696, Email: alessandro.prigione@mdc-berlin.de.

Anne Lombès, INSERM U1016, Institut Cochin, 24, rue du Fb St Jacques, Paris F-75014 France. Phone: 0033-1-53732753, Fax: 0033-1-44412421, Email: anne.lombes@inserm.fr.

Lead Contact: Alessandro Prigione (alessandro.prigione@mdc-berlin.de)

Keywords: neural progenitors; NPCs; iPSCs; mitochondrial disorders; mtDNA mutations; *MT-ATP6*, drug discovery.

Summary

Mitochondrial DNA (mtDNA) mutations frequently cause neurological diseases. Modeling of these defects has been difficult because of the challenges associated with engineering mtDNA. We show here that neural progenitor cells (NPCs) derived from human induced pluripotent stem cells (iPSCs) retain the parental mtDNA profile and exhibit a metabolic switch towards oxidative phosphorylation. NPCs derived in this way from patients carrying a deleterious homoplasmic mutation in the mitochondrial gene *MT-ATP6* (m.9185T>C) showed defective ATP production and abnormally high mitochondrial membrane potential (MMP), plus altered calcium homeostasis, which represents a potential cause of neural impairment. High-content screening of FDA-approved drugs using the MMP phenotype highlighted avanafil, which we found was able to partially rescue the calcium defect in patient NPCs and differentiated neurons. Overall, our results show that iPSC-derived NPCs provide an effective model for drug screening to target mtDNA disorders that affect the nervous system.

Introduction

Approximately 1 in 5,000 individuals (Gorman et al., 2015) suffer from deleterious mitochondrial DNA (mtDNA) mutations that can cause metabolic disorders and typically lead to dysfunctions of the nervous system (Carelli and Chan, 2014). Recent breakthroughs in the field of "mitochondrial medicine" might yield methods to prevent the transmission of pathogenic mtDNA mutations in the future (Mitalipov and Wolf, 2014; Reddy et al., 2015). But currently no cures or effective interventional therapies are available for patients who have already inherited the mutations and are subject to such disorders (Pfeffer et al., 2013).

The development of new treatment options has been hampered by a lack of relevant models for mtDNA-related diseases, largely due to the challenges of engineering mtDNA. mtDNA mutations can be introduced into mouse germ cells (Inoue et al., 2000) or can be induced to occur as a consequence of a proof-reading deficient DNA polymerase gamma (Kauppila et al., 2016). However, the generated mouse models cannot recapitulate the heteroplasmy or tissue-specificity of mtDNA disorders. The most important cellular models of mtDNA diseases are based on cytoplasmic hybrids (cybrids), obtained by fusing immortalized human cell lines depleted of mtDNA with patient-derived enucleated cells. These models have permitted the identification of some of the cellular and molecular consequences that follow from mutations in mtDNA (King and Attardi, 1989). But cybrids cannot address effects that result from the interplay between mitochondrial DNA and specific characteristics of an individual patient's nuclear DNA, which have been shown to influence the course of these diseases (Benit et al., 2010; D'Aurelio et al., 2010). Additionally, the bioenergetics of cybrids depend on glycolysis, whereas the neuronal cells that are symptomatic rely on mitochondrial oxidative phosphorylation (OXPHOS) (Abramov et al., 2010; Carelli and Chan, 2014). These significant differences limit the extent to which cybrids can be used as models in searching for new types of therapies.

Here we suggest an innovative, more potent alternative in the form of neural progenitor cells (NPCs), which have the characteristics needed in a model to study neurological diseases caused by mtDNA mutations and setting up drug discovery pipelines to treat them. NPCs can be rapidly obtained from induced pluripotent stem cells (iPSCs), either through an intermediate generation of rosettes (Koch et al., 2009) or the direct application of a cocktail of small molecules (Li et al., 2011; Reinhardt et al., 2013). We have previously shown that mitochondria undergo morphological and metabolic reconfigurations upon the generation of iPSCs (Prigione et al., 2010). Here we further demonstrate that when iPSCs are put through the steps of neural induction to become NPCs, their mitochondria undergo maturation and a metabolic shift towards neuronal-like oxidative metabolism, while entirely retaining the mitochondrial genome of the parent cell from which they were originally derived.

To examine whether NPCs represent a valid cellular system for compound screening approaches for mtDNA diseases, we generated iPSC-derived NPCs from three patients carrying the mutation m.9185T>C in the *MT-ATP6* gene for ATP synthase (Complex V) in a homoplasmic state (i.e. affecting all mtDNA molecules). This mutation is a recurrent cause of neurological diseases such as Leigh syndrome (Moslemi et al., 2005), NARP (Neuropathy, Ataxia, Retinitis Pigmentosa) (Childs et al., 2007), and episodic paralysis with spinal neuropathy (Aure et al., 2013). Patient-derived NPCs exhibited functional alterations including decreases in ATP production, abnormally increased mitochondrial membrane potential (MMP), and altered calcium homeostasis. We developed a high-content screening (HCS) strategy based on the patient MMP phenotype and used it to screen a library of FDA-approved compounds. The phosphodiesterase type 5 (PDE5) inhibitor avanafil, a compound that reduced the mitochondrial hyperpolarization, also partially rescued the calcium defect in both patient NPCs and differentiated neurons. These findings suggest that iPSC-derived NPCs can be used as an innovative model system to analyze mechanisms underlying mtDNA-

related neurological disorders and to carry out personalized phenotypic drug discovery for diseases that have been untreatable until now.

Results

Functional assessments of neural-induced neural progenitor cells (NI NPCs)

A small molecule-based protocol (Li et al., 2011) was used to facilitate neural induction (NI) of human pluripotent stem cells (PSCs), bypassing rosette derivation (Koch et al., 2009), which is time-consuming and operator-dependent **(Fig. S1A)**. Neural-induced neural progenitor cells (NI NPCs) were obtained from the human embryonic stem cell (hESC) lines H1 and H9, control iPSCs derived *via* transfection (TF) of episomal vectors, and control iPSC lines previously generated *via* retroviral transduction (TD) (Prigione et al., 2010; Prigione et al., 2011a; Prigione et al., 2011b) **(Fig. S1B-H)**. NI NPCs grew as a uniform monolayer, expressed NPC marker proteins, retained their multipotent identity for over 30 passages, and were capable of generating neuronal and glial subtypes including GABAergic neurons, dopaminergic neurons, and astrocytes **(Fig. 1A)**.

NI NPCs functionally responded to calcium mobilization, following voltage-dependent (high potassium chloride) and receptor-dependent (glutamate) stimuli **(Fig. 1B-E; Video S1)**. This led to the influx of calcium into the cells and subsequent calcium-induced calcium release from intracellular stores. In contrast, no response was provoked in either iPSCs or hESCs **(Fig. 1B-E)**. This suggested that NI NPCs might be suitable models for an investigation of calcium-regulated mechanisms. Whole cell patch clamp recordings in the current clamp mode were performed on NI NPCs and neurons at various time points of differentiation. In maturing neuronal-like cells, single and repetitive action potentials appeared after 8-12 weeks of differentiation **(Fig. S1I-J)**. Depolarizing currents failed to induce a firing of action potentials in NI NPCs **(Fig. 1F)**. Membrane potentials and resistance, on the other hand, did not change significantly upon differentiation (**Fig. 1G)**. This indicated

that although NI NPCs do not fire action potentials upon depolarization, their passive electrical properties are close to those of differentiated neuronal-like cells.

Principal component analysis (PCA) demonstrated that the transcriptome of NI NPCs was similar to that of NPCs generated using the traditional rosette-based approach (rNPCs) or obtained from *ex vivo* adult human brain (eNPCs) **(Fig. 1H; Fig S2A)**. This was also confirmed by comparing our data with previously published NPC transcriptomes (Brennand et al., 2011; Hargus et al., 2014; Li et al., 2011; Reinhardt et al., 2013; Stein et al., 2014) **(Fig. S2B)**. A pathway analysis of the uniquely expressed genes in NI NPCs, rNPCs, and eNPCs revealed that eNPCs exhibited a higher commitment towards neuronal development compared to the other PSC-derived NPCs **(Fig. S2C-D; Table S1)**. Nonetheless, NI NPCs, rNPCs, and eNPCs displayed a highly comparable pattern once mapped onto the human brain atlas **(Fig. 1I)**. Hence, PSC-derived NPCs may sufficiently represent NPCs that reside in the adult human brain.

NI NPCs exhibit mitochondrial maturation and neuronal-like energy metabolism

The generation of iPSCs is accompanied by an extensive restructuring of mitochondria and energy metabolism (Folmes et al., 2011; Prigione et al., 2010). A hierarchical clustering of genes involved in energy metabolism (Prigione et al., 2011b) identified differences in the metabolic regulation of PSCs and NPCs (including NI NPCs, rNPCs, and eNPCs) **(Fig. 1J)**. Clustering the samples according to OXPHOS genes produced the same pattern (data not shown). This suggests that NPCs may regulate cellular bioenergetics fundamentally differently from PSCs, irrespective of the mode by which they were derived. qPCR data confirmed that glycolytic regulators such as *GLUT3* and *PDK1*- were down-regulated in NPCs and neurons in comparison to PSCs, indicating that neural induction is accompanied by a reduction of glycolytic metabolism **(Fig. 1K)**.

Transmission electron microscopy showed that the mitochondria of NI NPCs display a fused ultrastructural morphology with well-developed cristae, resembling those of neurons but differing from the ultrastructure of PSC mitochondria. **(Fig. 2A).** In accordance, there was a significant increase in mitochondrial length during neural induction **(Fig. 2B)**.

We used seahorse technology, which concomitantly measures respiration (oxygen consumption rate, OCR) and glycolysis (extracellular acidification rate, ECAR), to compare the bioenergetic profiles of NI NPCs and neurons to those of PSCs and fibroblasts **(Fig. 2C-D)**. The rates of basal and maximal respiration and proton leak were similar in all cell types except fibroblasts, whose maximal respiration was higher **(Fig. S2E-G)**. Fibroblasts also had a much higher spare respiratory capacity than NI NPCs and neurons, in which the levels were only slightly higher than those of PSCs **(Fig. 2E)**. Conversely, NI NPCs and neurons experienced a sharp reduction in basal glycolysis compared to PSCs. This reduction was highly significant and more pronounced than that seen in fibroblasts **(Fig. 2F)**. This seems to indicate that neural induction is associated with a strong decrease of glycolytic metabolism. Accordingly, the OCR/ECAR ratio increased to a similar degree in fibroblasts, NI NPCs, and neurons compared to PSCs, suggesting a predominance of OXPHOS over glycolysis in these cell types **(Fig. 2G).** This finding was supported by the lower amounts of extracellular lactate found in NI NPCs and neurons than in PSCs **(Fig. 2H)**. The fact that NI NPCs could be maintained in glucose-free galactose medium, which requires using OXPHOS **(Fig 2I)**, is further evidence of a lower dependence on glycolysis.

These data suggest that neural induction triggers mitochondrial maturation, leading to an oxidative metabolic state in NI NPCs which resembles that of neurons.

NI NPCs retain their parental mtDNA sequence profile

To make useful models of mitochondrial diseases from NI NPCs, we needed to exclude the possibility that mtDNA had undergone changes during stages of induction, as can

happen in the generation of iPSCs (Ma et al., 2015; Prigione et al., 2011b). We performed Sanger sequencing of the entire mtDNA, using long-range PCR with nested primers to exclude nuclear mtDNA pseudogenes. We analyzed BJ control fibroblasts, BJ-derived TD-iPSCs, BJ-derived TF-iPSCs, hESCs, and the NI NPCs generated from the PSCs.

We found that the specific mtDNA variants from each individual were fully retained upon iPSC derivation, regardless of the reprogramming method that was used. This was also true upon neural induction **(Fig. 3A, Table S2)**, irrespective of the type of variant and its location within the mtDNA sequence **(Fig. 3B)**. Remarkably, even the spectrum of D310 tract heteroplasmy in the hypervariable region of the D-loop (mtDNA nt 57-372) was preserved through these stages **(Fig. 3C)** (its high heterogeneity makes it a common tool for forensic fingerprinting).

Finally, in contrast to a recent report on hESCs (Van Haute et al., 2013), we used two distinct long-range PCR protocols to dismiss the possibility that large mtDNA deletions had occurred in PSCs (including hESCs, TD-iPSCs and TF-iPSCs) or NI NPCs **(Fig. 3D)**. These results demonstrate that NI NPCs can maintain the mtDNA profile of the primary cells from which they are derived.

Generation of patient NI NPCs carrying a homoplasmic *MT-ATP6* mutation

NI NPCs may represent a *bona fide* model system for mtDNA-related neurological diseases because they share features with brain-derived neural cells **(Fig. 1I)**, rely on mitochondrial metabolism **(Fig. 2A-I)**, and retain the parental mtDNA profile **(Fig. 3A-D)**. To replicate these findings in a real-case scenario, we derived NI NPCs from three patients from a family that harbors the homoplasmic mutation m.9185T>C in the *MT-ATP6* gene (Aure et al., 2013) **(Fig. S3A-F)**. The cells, to which we assigned the common designation NPC_ATP6, comprised NI A1 (from the iPSC line TFA1), NI A2 (iPSC line TDA2.3), and NI A3 (iPSC line TDA3.1) and expressed the correct NPC protein markers **(Fig. 4A)**.

We used whole mtDNA sequencing and RFLP analysis to demonstrate that NPC_ATP6 retained the mtDNA of the original fibroblasts. The cells exhibited homoplasmic levels of the m.9185T>C mutation without any additional mtDNA mutations **(Fig. 4B-C; Fig. S4A-C)**. NPC_ATP6 also maintained intact versions of the parental D310 hypervariable regions of the D-loop and did not undergo any mtDNA deletions **(Fig. S4D-F)**. This means that any cellular phenotypes in NPC_ATP6 that are driven by the mitochondrial genome can be solely attributed to the patient-specific *MT-ATP6* mutation.

Bioenergetic consequences of the homoplasmic *MT-ATP6* mutation

Direct measurements of ATP production in permeabilized NPC_ATP6 cells revealed a significant defect **(Fig. 4D)** similar to that found in the primary fibroblasts from which they were obtained (Fib_ATP6) and in three independent cybrid clones derived from A1 fibroblasts (Cyb_ATP6) **(Fig. 4D)**. In spite of this, we found unaffected steady-state levels of ATP in intact NPC_ATP6, whether grown under standard conditions or after 4 hours in starvation medium, and in Fib_ATP6 and Cyb_ATP6 **(Fig. 4E)**. Accordingly, the reduced production of ATP in NPC_ATP6 did not affect the cells' metabolic profile under basal or starvation states as assessed with Seahorse technology **(Fig. S5A-D)** or their extracellular lactate content **(Fig S5E)**. This suggests that cells carrying the m.9185T>C mutation had efficiently adapted their energy expenditure to the lower levels of ATP. This behavior is also encountered in physiological conditions when there is an energy shortage (Staples and Buck, 2009), and is also in agreement with clinical observations (Campbell and Marcinek, 2016). One of the adjustments probably involves the partial depolarization of the plasma membrane (Aure et al., 2013), as we observed in NPC_ATP6 using electrophysiology analysis **(Fig. 4F)**.

The proliferation rates of NPC_ATP6, Fib_ATP6, and Cyb_ATP6 were likewise unaffected in glucose medium or during the shift of cellular metabolism towards OXPHOS in galactose medium **(Fig. 4G)**. NPC_ATP6 appeared to have normal mtDNA copy number,

(Fig. S5F) and mitochondrial ultrastructure and distribution **(Fig. S5G-H)**. Measurements of the kinetics of MitoSox signal revealed no change in the production of superoxide ions in NPC_ATP6 and Cyb_ATP6, in contrast to significant increases that have been previously observed in Fib_ATP6 **(Fig. 4H)** (Aure et al., 2013). These findings suggest that distinct cell types find different ways of responding to the same bioenergetic challenge. So in seeking the mechanisms responsible for the neural impairment associated with *MT-ATP6* mtDNA mutations, neural-like cells should be used (Abramov et al., 2010).

Mitochondrial hyperpolarization in neural cells carrying the *MT-ATP6* mutation

We next used a permeabilization-based method to measure the mitochondrial membrane potential (MMP) of NPC_ATP6, Fib_ATP6, and Cyb_ATP6. We observed an increase of MMP, as expected, in the presence of ADP, which is the substrate of ATP synthase that induces state 3 respiration **(Fig. S6A-C)**. Treating all permeabilized cells with oligomycin, an inhibitor of ATP synthase that induces state 4 respiration, revealed normal MMP **(Fig. S6A-C)**. Importantly, between state 3 and 4 respiration, individual NPC_ATP6 cells experienced a sharp decrease in MMP. **(Fig. 5A)**. The significance of the change was lower in mutant cybrids, and did not reach significance in patient fibroblasts **(Fig. 5A)**. This suggested that NPCs might not regulate MMP as efficiently as either fibroblasts or cybrids.

Next we carried out an imaging-based assessment of MMP in live, intact cells. This revealed a significant, abnormal increase in MMP in NPC_ATP6 cells, but not in Fib_ATP6 or Cyb_ATP6 **(Fig. 5B).** To control for technical bias, we demonstrated that oligomycin induced similar increases in the MMP signal in the three cell types **(Fig. S6D)**. Notably, neurons derived from patient NPCs (Neur_ATP6) also exhibited mitochondrial hyperpolarization **(Fig. 5C)**. We could exclude differentiation defects as the cause, since populations of Neur_ATP6 and control neurons (Neur_Ctrl) had a similar number of TUJ1-positive cells. **(Fig. 5D; Fig S6E)**. Furthermore, the mitochondria of Neur_ATP6 had normal

morphology and lengths compared to Neur_Ctrl **(Fig. 5E-F)**. This means that the phenotypes observed in differentiated neurons replicated those observed in NI NPCs, including the abnormal MMP increase.

MT-ATP6 mutation may thus specifically disrupt the ability of neural cells (including neural progenitor cells and post-mitotic neurons) to control MMP under basal conditions, an effect that is not seen in cybrids or fibroblasts.

Altered mitochondrial calcium homeostasis in NPC_ATP6

To gain further insights into the pathophysiology of the *MT-ATP6* mutation, we interrogated the global transcriptome of control and patient NPCs (**Table S1)**. We found a variable modulation of the expression of genes encoding for mitochondrial complexes, which supported our bioenergetic findings and excluded a uniform functional transcriptional compensatory response in NPC_ATP6 (**Fig S6F)**. On the other hand, genes involved in mitochondrial calcium homeostasis were consistently down-regulated in NPC_ATP6 **(Fig. S6G)**. A cluster analysis of these genes permitted us to observe patterns that clearly distinguished patient-derived NI NPCs from control NI NPCs. In particular, NPC_ATP6 showed significant down-regulation of *LETM1* in the inner mitochondrial membrane, *VDAC3* in the outer mitochondrial membrane, and *ATP5O*, which encodes for oligomycin sensitivity-conferring protein (OSCP) whose decreased expression is associated with enhanced sensitivity of the permeability transition pore (PTP) to calcium (Giorgio et al., 2013) **(Fig. 6B)**. These disease-specific patterns were not found in PSCs or fibroblasts, which makes sense because those cells do not develop symptoms in the diseases **(Fig. 6A).**

A global proteomics analysis confirmed that calcium homeostasis was likely being altered in NPC_ATP6s. A pair-wise analysis revealed a down-regulation of components of the "calcium signaling" pathway in all three patient NPC lines compared to control lines **(Fig. 6C)**. Additional pathways that were down-regulated in NPC_ATP6s related to the

“mitochondrial membrane” and “electron carrier activity” (**Fig. S6H**), while the “apoptosis” and “p53/hypoxia" pathways were up-regulated compared to controls (**Fig. S6I**).

Given the coherent picture of calcium dyshomeostasis from the "-omics" analyses, we set up calcium imaging experiments to pursue its functional relevance. Stimulating NPC_ATP6 cells with glutamate led to decreased calcium-induced calcium release from intracellular stores **(Fig. 6D; Video S2)**. To avoid effects dependent on the plasma membrane, which was partially depolarized in the patient cells **(Fig. 4F)**, we analyzed calcium homeostasis in permeabilized NI NPCs exposed to increasing doses of external calcium. NPC_ATP6 displayed a significant reduction in the acute increase of Fluo-4-labeled cytosolic calcium which occurred after the third calcium addition **(Fig. 6E)**. This was also the case following treatment with a combination of FCCP and antimycin A, which depolarizes the MMP leading to the release of mitochondrial calcium into the cytosol **(Fig. 6F)**. In contrast, treatment with thapsigargin, which blocks calcium uptake resulting into calcium release from the endoplasmic reticulum, induced a similar cytosolic calcium increase in both patient and control NPCs **(Fig. 6G)**.

Defects in the handling of calcium impair cellular functions, particularly in neuronal cells (Neher and Sakaba, 2008), which may help explain why symptoms arise specifically in the neurons of patients with ubiquitous *MT-ATP6* homoplasmic mutations. Moreover, the findings pointed to a specific alteration in mitochondrial calcium homeostasis, which is strongly influenced by the state of mitochondrial polarization (Rizzuto et al., 2012). This fits with our finding that Cyb_ATP6 achieves better MMP regulation **(Fig. 5A-B)** and exhibits normal calcium responses **(Fig. 6H-I)**.

Phenotypic compound screenings in NPC_ATP6

We next sought to address whether NPCs might be suitable for drug discovery approaches, targeting the aberrant MMP phenotype identified in patient NPCs and confirmed

in patient neurons. We adapted the imaging-based MMP assay to a 384-well plate format that could be used with the high-content screening (HCS) automated fluorescence microscope Cellomics ArrayScan **(Fig. 7A)**. As a proof-of-concept, we tested 130 compounds from a library of 700 FDA-approved drugs **(Table S3)** for effects on the cells' MMP. In order to overcome a degree of variability inherent to the assay, we used each compound in duplicate and repeated the same screening twice. To reduce the risk of false negatives, we focused on NI A2, the NPC_ATP6 line with the highest MMP. Each compound was used at a final concentration of 1 µM and was dissolved in 0.04% DMSO, a dose that we verified as non-toxic and with no direct influence on the MMP **(Fig. S7A-B)**. Ten compounds decreased the MMP of NI A2 down to -2 standard deviation values **(Fig. 7B)** without negatively affecting the cells' viability **(Fig. S7C-D)**.

We decided to focus on one of these compounds: avanafil **(Fig. 7B)**, a phosphodiesterase type 5 (PDE5) inhibitor. The family of compounds to which this belongs is commonly used against erectile dysfunction in adults and is approved for pediatric use to treat pulmonary arterial hypertension (Archer and Michelakis, 2009). These compounds can cross the blood brain barrier and have been reported to have positive effects on neurogenesis (Garcia-Barroso et al., 2013; Rutten et al., 2008). We assessed avanafil's impact on bioenergetics and calcium homeostasis in patient-derived NPCs and differentiated neurons. Treatment with 1 µM avanafil overnight induced a slight but significant depolarization of mitochondria, similar to that seen in state 3 and state 4 respiration **(Fig. S7E-F)**. Despite this partial depolarization, there was no significant change in the rate of ATP production in NPC_ATP6 **(Fig. 7C)**. The ATP steady-state level remained constant also in patient neurons after exposure to the drug **(Fig. 7D).**

Avanafil did not alter the profile of cytosolic calcium in NPC_ATP6 when increasing doses of external calcium were applied **(Fig. 7E-F)**. Importantly, however, the overnight treatment with avanafil increased the release of mitochondrial calcium when we triggered

mitochondrial depolarization using FCCP and antimycin A in the three NPC_ATP6 lines, reaching significance in two of them **(Fig. 7G-H)**. Avanil also induced a similar increase in mitochondrial calcium release in differentiated neurons carrying the *MT-ATP6* mutation **(Fig. 7I-J)**.

Overall, these data demonstrate that NI NPCs can be successfully used in phenotypic compound screenings with the aim of developing personalized drug discovery approaches for neurological mtDNA diseases **(Fig. S7G)**.

Discussion

Technical and methodological limitations have impeded the development of models for the development of individualized approaches to diseases caused by mutations in mitochondrial genes. Here we describe an innovative system based on iPSC-derived NPCs that can be used both to discover the cellular mechanisms that these mutations disrupt and develop novel treatments based on screens or other methods.

We show that NPCs undergo functional mitochondrial maturation and develop oxidative metabolism in a way that resembles normal neuronal development. During this process, the cells preserve the patient-specific nuclear and mitochondrial matched genotypes. This is crucial in the study of mtDNA disorders, given that the nuclear background is thought to play a modulatory role in in these diseases (Benit et al., 2010; D'Aurelio et al., 2010), as illustrated by the phenotypic differences associated with the same homoplasmic *MT-ATP6* mutation (Aure et al., 2013; Pitceathly et al., 2012). Hence, NPCs should be useful in dissecting the specific vulnerability of the nervous system to mtDNA diseases (Abramov et al., 2010; Carelli and Chan, 2014).

The approach described here for a homoplasmic mtDNA mutation should be equally applicable to heteroplasmic mutations. In fact, iPSC-derived NPCs retained the entire mtDNA profile of the initial fibroblasts, including even the hypervariable D-loop region. Studies have

indicated that the induction to iPSCs may be associated with heteroplasmic mtDNA alterations (Folmes et al., 2013; Hamalainen et al., 2013; Perales-Clemente et al., 2016; Prigione et al., 2011b). These variations appear to derive from the clonal origin of the iPSCs, because they also occur in clonally-expanded fibroblasts (Kang et al., 2016; Ma et al., 2015). This means that the mtDNA sequence profile of patient-derived iPSC lines must be thoroughly assessed to ensure that the cells are suitable for use in drug discovery or other types of treatments.

Our finding that the *MT-ATP6* mutation disrupted mitochondrial calcium homeostasis specifically in NPCs but not in fibroblasts or cybrids may help explain the specificity of the defects it causes. Neuronal cells are particularly sensitive to changes in calcium handling (Neher and Sakaba, 2008), which is considered a major contributor to excitotoxic cell death (Orrenius et al., 2003). The occurrence of aberrantly reduced cytoplasmic calcium in NPC_ATP6 cells might also explain the beneficial effects observed when patients carrying the *MT-ATP6* mutation are treated with acetazolamide (Aure et al., 2013). Acetazolamide activates calcium-activated potassium [K_{Ca}] plasma membrane channels, whose opening is hindered by reductions in the amount of cytosolic calcium (Sah and Faber, 2002). Our new data imply that targeting the MMP, which lies "upstream" of calcium dyshomeostasis, may be a useful strategy to address the neural impairment that develops through the mutation **(Fig. 7K)**. This fits with results from cellular and animal models, which showed that mild uncouplers can improve neural calcium homeostasis (Maragos and Korde, 2004).

Further work is needed to dissect the mechanisms responsible for the disruption of mitochondrial calcium homeostasis in NPC_ATP6 cells. Mitochondrial hyperpolarization, which promotes the sequestration of calcium into mitochondria (Rizzuto et al., 2012), might be responsible for the reduced mitochondrial calcium release observed in the cytoplasm. Another possibility is an impairment in the regulation of mitochondrial calcium efflux

mechanisms such as the sodium calcium exchanger (NCX) or the permeability transition pore (PTP), which consists of dimers of ATP synthase (Giorgio et al., 2013) **(Fig. 7K).**

We also carried out the first phenotypic small molecule screening in patient-derived NPCs, which led to our identification of the PDE5 inhibitor avanafil as a potential therapeutic agent for use in *MT-ATP6*-related encephalopathies. PDE5 inhibitors increase the intracellular level of cyclic GMP (cGMP), which in turn activates [K_{Ca}] channels in both the plasma membrane and the inner mitochondrial membrane (Ahern et al., 2002; Szewczyk et al., 2006; Wang et al., 2008). The positive effects of avanafil on calcium homeostasis may thus be due to its effects on cellular polarization, which are similar to those of acetazolamide, and/or to its triggering of a slight mitochondrial depolarization, which would direct influence mitochondrial calcium homeostasis **(Fig. 7K)**. Yet another possibility is that PDE5 inhibitors affect the opening of the PTP (Ascah et al., 2011). Further studies will be needed to clarify the mode by which avanafil and PDE5 inhibitors act in the context of *MT-ATP6*-associated neural impairment. Future work will also determine whether the compounds we have identified can also target mechanisms involved in other mitochondrial disorders.

In conclusion, iPSC-derived NPCs appear well suited for use in drug screening strategies aimed at developing treatments for neurological mitochondrial disorders. Live cell-based HCS permits the simultaneous evaluation of mitochondrial parameters beyond MMP (Iannetti et al., 2016), and might allow compound screenings aimed simultaneously at multiple mitochondrial phenotypes. The employment of FDA-approved libraries could speed up the process of translation to clinical applications through drug repositioning (Ashburn and Thor, 2004). We believe that creating disease-relevant *in vitro* model systems such as the one described here may represent an essential step toward the identification of effective therapies for mtDNA diseases and other conditions that cannot yet be treated.

Author contributions

Conceptualization, A.P. and A.L.; Methodology, A.P. A.L., C.L., P.L., R.B., B.W, T.M., D.M., B.W., J.C.M., and M.Sc.; Formal Analysis, M.Si., B.M., and N.M.; Investigation, A.L., M.Sc., C.L., P.L., R.B., A.Z., G.I., K.A., M.L., O.Z., E-M.L., V.P., B.F., J.E., M.Se., B.M. and D.M.; Resources, N.H.; Writing –Original Draft, A.P. and A.L.; Writing – Review & Editing, A.P. and A.L.; Supervision, A.P., A.L., M.Sc., Z.I., J.C.M., J.P., F.B., J.A., and E.E.W.; Visualization, C.L., A.P., and A.L; Funding Acquisition, A.P., A.L., and M.Sc.

Acknowledgements

The authors declare no competing financial or commercial interests. We thank Dr. Sarah Doss (Charité – Universitätsmedizin Berlin) for providing the control fibroblast lines Con1 and Con2, Clemens Edler (MPI-MG) for TrakEM2 analysis, Dr. Thomas Wiglenda (MDC) for essential advice with compound screening preparation, Franziska Seifert (Charité – Universitätsmedizin Berlin) for help in long-range PCRs, Beate Lukaszewska-McGreal (MPI-MG) for proteomic sample preparation, and Franziska Wiedemann (MDC) for cell culture and technical support. We are grateful to Russ Hodge (MDC) for proofreading the manuscript. We acknowledge support from the MDC (PhD fellowship to R.B. and BOOST Idea Competition Award to A.P.), the Deutsche Forschungsgemeinschaft (DFG) (PR1527/1-1 & SCHU1187/4-1 to A.P. and M.Sc.; Neurocure Exc 257 to M.Sc.; Priority Programme SPP 1784 ME2075/7-1 to J.C.M.), the Berlin Institute of Health (BIH) (to A.P. and M.Sc. in form of a PhD fellowship to C.L.; to J.P. and E.E.W. as Collaborative Research Grant; to B.M. as Gender Equality Funds), the Fondation pour la Recherche Médicale (FRM) (grant DPM20121125550 to A.L. and A.P. in form of financial support and post-doctoral fellowship to P.L.), the AFM Telethon (to A.P. and A.L.), the Fritz Thyssen Foundation (Az.10.11.2.160 to A.P.), and the Bundesministerium für Bildung und Forschung (BMBF) (e:Bio young investigator grant AZ.031A318 to A.P.; ERA-Net Neuron II project CIPRESS to J.C.M.; AERIAL P1 to J.P.).

References

Abramov, A.Y., Smulders-Srinivasan, T.K., Kirby, D.M., Acin-Perez, R., Enriquez, J.A., Lightowlers, R.N., Duchen, M.R., and Turnbull, D.M. (2010). Mechanism of neurodegeneration of neurons with mitochondrial DNA mutations. Brain *133*, 797-807.

Ahern, G.P., Klyachko, V.A., and Jackson, M.B. (2002). cGMP and S-nitrosylation: two routes for modulation of neuronal excitability by NO. Trends in neurosciences *25*, 510-517.

Archer, S.L., and Michelakis, E.D. (2009). Phosphodiesterase type 5 inhibitors for pulmonary arterial hypertension. The New England journal of medicine *361*, 1864-1871.

Ascah, A., Khairallah, M., Daussin, F., Bourcier-Lucas, C., Godin, R., Allen, B.G., Petrof, B.J., Des Rosiers, C., and Burelle, Y. (2011). Stress-induced opening of the permeability transition pore in the dystrophin-deficient heart is attenuated by acute treatment with sildenafil. American journal of physiology Heart and circulatory physiology *300*, H144-153.

Ashburn, T.T., and Thor, K.B. (2004). Drug repositioning: identifying and developing new uses for existing drugs. Nat Rev Drug Discov *3*, 673-683.

Aure, K., Dubourg, O., Jardel, C., Clarysse, L., Sternberg, D., Fournier, E., Laforet, P., Streichenberger, N., Petiot, P., Gervais-Bernard, H., *et al.* (2013). Episodic weakness due to mitochondrial DNA MT-ATP6/8 mutations. Neurology *81*, 1810-1818.

Benit, P., El-Khoury, R., Schiff, M., Sainsard-Chanet, A., and Rustin, P. (2010). Genetic background influences mitochondrial function: modeling mitochondrial disease for therapeutic development. Trends in molecular medicine *16*, 210-217.

Brennand, K.J., Simone, A., Jou, J., Gelboin-Burkhart, C., Tran, N., Sangar, S., Li, Y., Mu, Y., Chen, G., Yu, D., *et al.* (2011). Modelling schizophrenia using human induced pluripotent stem cells. Nature *473*, 221-225.

Campbell, M.D., and Marcinek, D.J. (2016). Evaluation of in vivo mitochondrial bioenergetics in skeletal muscle using NMR and optical methods. Biochim Biophys Acta *1862*, 716-724.

Cardona, A., Saalfeld, S., Schindelin, J., Arganda-Carreras, I., Preibisch, S., Longair, M., Tomancak, P., Hartenstein, V., and Douglas, R.J. (2012). TrakEM2 software for neural circuit reconstruction. PLoS One *7*, e38011.

Carelli, V., and Chan, D.C. (2014). Mitochondrial DNA: impacting central and peripheral nervous systems. Neuron *84*, 1126-1142.

Childs, A.M., Hutchin, T., Pysden, K., Highet, L., Bamford, J., Livingston, J., and Crow, Y.J. (2007). Variable phenotype including Leigh syndrome with a 9185T>C mutation in the MTATP6 gene. Neuropediatrics *38*, 313-316.

Cox, J., Hein, M.Y., Luber, C.A., Paron, I., Nagaraj, N., and Mann, M. (2014). Accurate proteome-wide label-free quantification by delayed normalization and maximal peptide ratio extraction, termed MaxLFQ. Molecular & cellular proteomics : MCP *13*, 2513-2526.

Cox, J., and Mann, M. (2008). MaxQuant enables high peptide identification rates, individualized p.p.b.-range mass accuracies and proteome-wide protein quantification. Nat Biotechnol *26*, 1367-1372.

D'Aurelio, M., Vives-Bauza, C., Davidson, M.M., and Manfredi, G. (2010). Mitochondrial DNA background modifies the bioenergetics of NARP/MILS ATP6 mutant cells. Hum Mol Genet *19*, 374-386.

Deschauer, M., Krasnianski, A., Zierz, S., and Taylor, R.W. (2004). False-positive diagnosis of a single, large-scale mitochondrial DNA deletion by Southern blot analysis: the role of neutral polymorphisms. Genetic testing *8*, 395-399.

Detjen, A.K., Tinschert, S., Kaufmann, D., Algermissen, B., Nurnberg, P., and Schuelke, M. (2007). Analysis of mitochondrial DNA in discordant monozygotic twins with

neurofibromatosis type 1. Twin research and human genetics : the official journal of the International Society for Twin Studies *10*, 486-495.

Folmes, C.D., Martinez-Fernandez, A., Perales-Clemente, E., Li, X., McDonald, A., Oglesbee, D., Hrstka, S.C., Perez-Terzic, C., Terzic, A., and Nelson, T.J. (2013). Disease-causing mitochondrial heteroplasmy segregated within induced pluripotent stem cell clones derived from a patient with MELAS. Stem Cells *31*, 1298-1308.

Folmes, C.D., Nelson, T.J., Martinez-Fernandez, A., Arrell, D.K., Lindor, J.Z., Dzeja, P.P., Ikeda, Y., Perez-Terzic, C., and Terzic, A. (2011). Somatic oxidative bioenergetics transitions into pluripotency-dependent glycolysis to facilitate nuclear reprogramming. Cell Metab *14*, 264-271.

Gandhi, S., Wood-Kaczmar, A., Yao, Z., Plun-Favreau, H., Deas, E., Klupsch, K., Downward, J., Latchman, D.S., Tabrizi, S.J., Wood, N.W., *et al.* (2009). PINK1-associated Parkinson's disease is caused by neuronal vulnerability to calcium-induced cell death. Mol Cell *33*, 627-638.

Garcia-Barroso, C., Ricobaraza, A., Pascual-Lucas, M., Unceta, N., Rico, A.J., Goicolea, M.A., Salles, J., Lanciego, J.L., Oyarzabal, J., Franco, R., *et al.* (2013). Tadalafil crosses the blood-brain barrier and reverses cognitive dysfunction in a mouse model of AD. Neuropharmacology *64*, 114-123.

Giorgio, V., von Stockum, S., Antoniel, M., Fabbro, A., Fogolari, F., Forte, M., Glick, G.D., Petronilli, V., Zoratti, M., Szabo, I., *et al.* (2013). Dimers of mitochondrial ATP synthase form the permeability transition pore. Proc Natl Acad Sci U S A *110*, 5887-5892.

Gorman, G.S., Schaefer, A.M., Ng, Y., Gomez, N., Blakely, E.L., Alston, C.L., Feeney, C., Horvath, R., Yu-Wai-Man, P., Chinnery, P.F., *et al.* (2015). Prevalence of nuclear and mitochondrial DNA mutations related to adult mitochondrial disease. Ann Neurol *77*, 753-759.

Hamalainen, R.H., Manninen, T., Koivumaki, H., Kislin, M., Otonkoski, T., and Suomalainen, A. (2013). Tissue- and cell-type-specific manifestations of heteroplasmic mtDNA 3243A>G mutation in human induced pluripotent stem cell-derived disease model. Proc Natl Acad Sci U S A *110*, E3622-3630.

Hargus, G., Ehrlich, M., Arauzo-Bravo, M.J., Hemmer, K., Hallmann, A.L., Reinhardt, P., Kim, K.P., Adachi, K., Santourlidis, S., Ghanjati, F., *et al.* (2014). Origin-dependent neural cell identities in differentiated human iPSCs in vitro and after transplantation into the mouse brain. Cell Rep *8*, 1697-1703.

Hazkani-Covo, E., Zeller, R.M., and Martin, W. (2010). Molecular poltergeists: mitochondrial DNA copies (numts) in sequenced nuclear genomes. PLoS Genet *6*, e1000834.

Iannetti, E.F., Smeitink, J.A., Beyrath, J., Willems, P.H., and Koopman, W.J. (2016). Multiplexed high-content analysis of mitochondrial morphofunction using live-cell microscopy. Nature protocols *11*, 1693-1710.

Inoue, K., Nakada, K., Ogura, A., Isobe, K., Goto, Y., Nonaka, I., and Hayashi, J.I. (2000). Generation of mice with mitochondrial dysfunction by introducing mouse mtDNA carrying a deletion into zygotes. Nat Genet *26*, 176-181.

Kang, E., Wang, X., Tippner-Hedges, R., Ma, H., Folmes, C.D., Gutierrez, N.M., Lee, Y., Van Dyken, C., Ahmed, R., Li, Y., *et al.* (2016). Age-Related Accumulation of Somatic Mitochondrial DNA Mutations in Adult-Derived Human iPSCs. Cell Stem Cell *18*, 625-636.

Kauppila, J.H., Baines, H.L., Bratic, A., Simard, M.L., Freyer, C., Mourier, A., Stamp, C., Filograna, R., Larsson, N.G., Greaves, L.C., *et al.* (2016). A Phenotype-Driven Approach to Generate Mouse Models with Pathogenic mtDNA Mutations Causing Mitochondrial Disease. Cell Rep *16*, 2980-2990.

Kirches, E., Michael, M., Warich-Kirches, M., Schneider, T., Weis, S., Krause, G., Mawrin, C., and Dietzmann, K. (2001). Heterogeneous tissue distribution of a mitochondrial

DNA polymorphism in heteroplasmic subjects without mitochondrial disorders. Journal of medical genetics *38*, 312-317.

Koch, P., Opitz, T., Steinbeck, J.A., Ladewig, J., and Brustle, O. (2009). A rosette-type, self-renewing human ES cell-derived neural stem cell with potential for in vitro instruction and synaptic integration. Proc Natl Acad Sci U S A *106*, 3225-3230.

Krencik, R., and Zhang, S.C. (2011). Directed differentiation of functional astroglial subtypes from human pluripotent stem cells. Nature protocols *6*, 1710-1717.

Kulak, N.A., Pichler, G., Paron, I., Nagaraj, N., and Mann, M. (2014). Minimal, encapsulated proteomic-sample processing applied to copy-number estimation in eukaryotic cells. Nat Methods *11*, 319-324.

Li, W., Sun, W., Zhang, Y., Wei, W., Ambasudhan, R., Xia, P., Talantova, M., Lin, T., Kim, J., Wang, X., *et al.* (2011). Rapid induction and long-term self-renewal of primitive neural precursors from human embryonic stem cells by small molecule inhibitors. Proc Natl Acad Sci U S A *108*, 8299-8304.

Ma, H., Folmes, C.D., Wu, J., Morey, R., Mora-Castilla, S., Ocampo, A., Ma, L., Poulton, J., Wang, X., Ahmed, R., *et al.* (2015). Metabolic rescue in pluripotent cells from patients with mtDNA disease. Nature *524*, 234-238.

Maragos, W.F., and Korde, A.S. (2004). Mitochondrial uncoupling as a potential therapeutic target in acute central nervous system injury. J Neurochem *91*, 257-262.

Mitalipov, S., and Wolf, D.P. (2014). Clinical and ethical implications of mitochondrial gene transfer. Trends in endocrinology and metabolism: TEM *25*, 5-7.

Moslemi, A.R., Darin, N., Tulinius, M., Oldfors, A., and Holme, E. (2005). Two new mutations in the MTATP6 gene associated with Leigh syndrome. Neuropediatrics *36*, 314-318.

Neher, E., and Sakaba, T. (2008). Multiple roles of calcium ions in the regulation of neurotransmitter release. Neuron *59*, 861-872.

Orrenius, S., Zhivotovsky, B., and Nicotera, P. (2003). Regulation of cell death: the calcium-apoptosis link. Nature reviews Molecular cell biology *4*, 552-565.

Perales-Clemente, E., Cook, A.N., Evans, J.M., Roellinger, S., Secreto, F., Emmanuele, V., Oglesbee, D., Mootha, V.K., Hirano, M., Schon, E.A., *et al.* (2016). Natural underlying mtDNA heteroplasmy as a potential source of intra-person hiPSC variability. EMBO J *35*, 1979-1990.

Pfeffer, G., Horvath, R., Klopstock, T., Mootha, V.K., Suomalainen, A., Koene, S., Hirano, M., Zeviani, M., Bindoff, L.A., Yu-Wai-Man, P., *et al.* (2013). New treatments for mitochondrial disease-no time to drop our standards. Nature reviews Neurology *9*, 474-481.

Pfiffer, V., and Prigione, A. (2015). Assessing the bioenergetic profile of human pluripotent stem cells. Methods Mol Biol *1264*, 279-288.

Pitceathly, R.D., Murphy, S.M., Cottenie, E., Chalasani, A., Sweeney, M.G., Woodward, C., Mudanohwo, E.E., Hargreaves, I., Heales, S., Land, J., *et al.* (2012). Genetic dysfunction of MT-ATP6 causes axonal Charcot-Marie-Tooth disease. Neurology *79*, 1145-1154.

Polster, B.M., Nicholls, D.G., Ge, S.X., and Roelofs, B.A. (2014). Use of potentiometric fluorophores in the measurement of mitochondrial reactive oxygen species. Methods in enzymology *547*, 225-250.

Prigione, A., Fauler, B., Lurz, R., Lehrach, H., and Adjaye, J. (2010). The senescence-related mitochondrial/oxidative stress pathway is repressed in human induced pluripotent stem cells. Stem Cells *28*, 721-733.

Prigione, A., Hossini, A.M., Lichtner, B., Serin, A., Fauler, B., Megges, M., Lurz, R., Lehrach, H., Makrantonaki, E., Zouboulis, C.C., *et al.* (2011a). Mitochondrial-associated cell death mechanisms are reset to an embryonic-like state in aged donor-derived iPS cells harboring chromosomal aberrations. PLoS One *6*, e27352.

Prigione, A., Lichtner, B., Kuhl, H., Struys, E.A., Wamelink, M., Lehrach, H., Ralser, M., Timmermann, B., and Adjaye, J. (2011b). Human induced pluripotent stem cells harbor homoplasmic and heteroplasmic mitochondrial DNA mutations while maintaining human embryonic stem cell-like metabolic reprogramming. Stem Cells *29*, 1338-1348.

Prigione, A., Rohwer, N., Hoffmann, S., Mlody, B., Drews, K., Bukowiecki, R., Blumlein, K., Wanker, E.E., Ralser, M., Cramer, T., *et al.* (2014). HIF1alpha modulates cell fate reprogramming through early glycolytic shift and upregulation of PDK1-3 and PKM2. Stem Cells *32*, 364-376.

Reddy, P., Ocampo, A., Suzuki, K., Luo, J., Bacman, S.R., Williams, S.L., Sugawara, A., Okamura, D., Tsunekawa, Y., Wu, J., *et al.* (2015). Selective elimination of mitochondrial mutations in the germline by genome editing. Cell *161*, 459-469.

Reinhardt, P., Glatza, M., Hemmer, K., Tsytsyura, Y., Thiel, C.S., Hoing, S., Moritz, S., Parga, J.A., Wagner, L., Bruder, J.M., *et al.* (2013). Derivation and expansion using only small molecules of human neural progenitors for neurodegenerative disease modeling. PLoS One *8*, e59252.

Rizzuto, R., De Stefani, D., Raffaello, A., and Mammucari, C. (2012). Mitochondria as sensors and regulators of calcium signalling. Nature reviews Molecular cell biology *13*, 566-578.

Rutten, K., Basile, J.L., Prickaerts, J., Blokland, A., and Vivian, J.A. (2008). Selective PDE inhibitors rolipram and sildenafil improve object retrieval performance in adult cynomolgus macaques. Psychopharmacology *196*, 643-648.

Sah, P., and Faber, E.S. (2002). Channels underlying neuronal calcium-activated potassium currents. Progress in neurobiology *66*, 345-353.

Staples, J.F., and Buck, L.T. (2009). Matching cellular metabolic supply and demand in energy-stressed animals. Comparative biochemistry and physiology Part A, Molecular & integrative physiology *153*, 95-105.

Stein, J.L., de la Torre-Ubieta, L., Tian, Y., Parikshak, N.N., Hernandez, I.A., Marchetto, M.C., Baker, D.K., Lu, D., Hinman, C.R., Lowe, J.K., *et al.* (2014). A quantitative framework to evaluate modeling of cortical development by neural stem cells. Neuron *83*, 69-86.

Subramanian, A., Tamayo, P., Mootha, V.K., Mukherjee, S., Ebert, B.L., Gillette, M.A., Paulovich, A., Pomeroy, S.L., Golub, T.R., Lander, E.S., *et al.* (2005). Gene set enrichment analysis: a knowledge-based approach for interpreting genome-wide expression profiles. Proc Natl Acad Sci U S A *102*, 15545-15550.

Szewczyk, A., Skalska, J., Glab, M., Kulawiak, B., Malinska, D., Koszela-Piotrowska, I., and Kunz, W.S. (2006). Mitochondrial potassium channels: from pharmacology to function. Biochim Biophys Acta *1757*, 715-720.

Van Haute, L., Spits, C., Geens, M., Seneca, S., and Sermon, K. (2013). Human embryonic stem cells commonly display large mitochondrial DNA deletions. Nat Biotechnol *31*, 20-23.

Vizcaino, J.A., Cote, R.G., Csordas, A., Dianes, J.A., Fabregat, A., Foster, J.M., Griss, J., Alpi, E., Birim, M., Contell, J., *et al.* (2013). The PRoteomics IDEntifications (PRIDE) database and associated tools: status in 2013. Nucleic Acids Res *41*, D1063-1069.

Wang, X., Fisher, P.W., Xi, L., and Kukreja, R.C. (2008). Essential role of mitochondrial Ca2+-activated and ATP-sensitive K+ channels in sildenafil-induced late cardioprotection. Journal of molecular and cellular cardiology *44*, 105-113.

Yu, J., Chau, K.F., Vodyanik, M.A., Jiang, J., and Jiang, Y. (2011). Efficient feeder-free episomal reprogramming with small molecules. PLoS One *6*, e17557.

Figure legends

Figure 1. Generation of NI NPCs. (A) Upper panel, spiked morphology of NI NPCs and expression of NPC markers PAX6, SOX2, NESTIN, DACH1, and HES5. Lower panel,

neurospheres from NI NPCs and differentiated neurons (TUJ1-positive), including dopaminergic (TH-positive) and GABAergic neurons (GABA-positive), and astrocytes (GFAP-positive). Scale bar: 100 µm. **(B)** Representative images of NI NPCs (line NI H1) showing cytosolic calcium before stimulation and at maximal peak Fluo-4 fluorescence after 1 mM glutamate (Glu) stimulus. Scale bar: 50 µm. **(C-D)** Cytosolic calcium monitored in PSCs and NI NPCs following voltage-mediated (30 mM KCl) and receptor-mediated (1 mM glutamate, Glu) stimuli. Time-point zero corresponds to stimuli administration. The profiles represent the average of PSCs (H1, H9, TFBJ) and corresponding NI NPCs (three biological replicates each). **(E)** Calcium responses were quantified by determining the area under the curve (AUC) of Fluo-4 fluorescence profiles. **(F)** Patch clamp recordings in NI NPCs and neurons and the effect of 100 nM tetrodotoxin (TTX) (shown here for line NI H1). **(G)** Membrane resistance (R_N) and membrane potential ($-V_m$) during the course of differentiation (from NI H1 and NI TFBJ). Populations were separated in "none" (n=21 out of three biological replicates), "single" (n=13), and "repetitive" (n=6) action potential firing cells. **(H)** Principal component analysis (PCA) showing the transcriptomic clustering of fibroblasts (BJ, HFF1), hESCs (H1, H9), iPSCs (TFBJ, TDBJ5, TDHFF1), NI NPCs (NI H1, NI H9, NI TDBJ5, NI TFBJ), rNPCs, and eNPCs. Probe-sets were filtered for at least one present call and with an IQR> 25th percentile. **(I)** Mapping of the transcriptomic data of NI NPCs, eNPCs and rNPCs onto the Allen Human Brain Atlas. Color key displays the range of pairwise ranked correlation between analyzed sample matrix. Columns designate different time periods in the pre- and postnatal phase (wpc: week post-conception) and rows specify brain areas (AMY: amygdala, FC: frontal cortex, HIP: hippocampus, M1C: primary motor cortex). **(J)** Clustering performed using genes known to regulate energy metabolism. **(K)** qPCR expression analysis of two glycolytic regulators in fibroblasts (BJ, HFF1), NI NPCs (NI H1, NI H9, NI TDBJ5, NI TFBJ), rNPCs, eNPCs, and neurons (from NI H1 and NI

TFBJ). Values are presented as Log2 of the ratio between the expression values of *GLUT3* or *PDK1* over *ACTB* in relation to the undifferentiated PSC line H1.

See also Figure S1, Figure S2, Table S1, and Video S1.

Figure 2. Mitochondrial and metabolic reconfiguration upon neural induction. (A) Transmission electron microscopy (TEM) images showing the morphology of mitochondria within PSCs, NI NPCs, and differentiated neurons (shown are H1, NI H1, and neurons from NI H1). Scale bar: 500 nm. **(B)** Mitochondrial length quantified in PSCs (H1, H9, TDHFF1, TDBJ4, TDBJ5, TFBJ), NI NPCs (NI H1, NI H9, NI TDBJ5, NI TFBJ), and neurons (from NI TFBJ) (at least 60 mitochondria per cell line, out of at least 20 TEM images). **(C)** Oxygen consumption rate (OCR) profile using the Seahorse XF24 Analyzer for PSCs (H1, H9, TFBJ), fibroblasts (BJ, HFF1), NI NPCs (NI H1, NI H9, NI TFBJ), and neurons (from NI H1 and NI TFBJ) (at least two biological replicates per line, each with at least three technical replicates). Olig: 1 µM oligomycin; FCCP: 1 µM FCCP; R+AntA: 1 µM rotenone + 1 µM antimycin A. **(D)** Extracellular acidification rate (ECAR) profile, reflecting glycolytic activity, measured in parallel to OCR. **(E-G)** Spare respiratory capacity (shown in relation to PSCs), basal glycolysis, and OCR/ECAR ratio were calculated from the Seahorse profiling. Statistics refer to PSCs. **(H)** Extracellular lactate content in PSCs (H1, H9, TFBJ), fibroblasts (BJ, HFF1), NI NPCs (NI H1, NI H9, NI TFBJ), and neurons (from NI H1 and NI TFBJ) (at least two biological replicates per line, each with at least seven technical replicates). **(I)** Cellular proliferation in 25 mM glucose (+ glucose) or in 10 mM galactose (- glucose + galactose) for PSCs (H1, TFBJ), NI NPCs (NI H1, NI H9, NI TFC1), fibroblasts (BJ, HFF1) (at least two biological replicates per line, each with at least three technical replicates) (error bars represent SD). In all panels, unless otherwise indicated, error bars represent SEM and p values were determined by unpaired two-tailed Student's t-tests: *P≤0.05, **P≤0.01, ***P≤0.001.

See also Figure S2.

Figure 3. Preservation of mtDNA during reprogramming and neural induction. (A) Number of variants identified with whole mtDNA sequencing in fibroblasts (black), PSCs (red), and NI NPCs (blue). **(B)** Location of mtDNA variants (green ovals) in BJ fibroblasts (black circle), BJ-derived iPSC line TDBJ5 (red circle), and TDBJ5-derived NI TDBJ5 (blue circle). **(C)** Preservation of the D310 tract heteroplasmy within the hypervariable region of the D-loop (mtDNA nt 57-372) in two hESCs and their related NI NPCs, in BJ fibroblasts, BJ-derived retroviral-based (TDBJ4 and TDBJ5) and plasmid-based (TFBJ and TFBJ.2) iPSC lines, and their respective NI NPCs. **(D)** Two different long-range PCR sets used to detect mtDNA deletions within PSCs and related NI NPCs.
See also Table S2.

Figure 4. Generation of NPC_ATP6 harboring the mutation m.9185T>C. (A) NPC markers, SOX2, NESTIN and PAX6, and proliferation marker Ki-67 in NPC_ATP6. Scale bar: 100 µm. **(B)** Whole mtDNA Sanger sequencing shown for the area around the mutation m.9185T>C for patient A2 in fibroblasts, iPSCs, and NPCs. **(C)** RFLP analysis confirming homoplasmic m.9185T>C mutation as a single 120 bp fragment (in control cells the restriction enzyme generates a 90 bp and a 30 bp fragment); WT: wild-type plasmid; Mut: mutant plasmid. **(D)** ATP production in permeabilized NPC_Ctrl (NI H1, NI H9, NI TDBJ5, NI TFBJ, NI TFC1, NI TFLR), NPC_ATP6 (NI A1, NI A2, NI A3), Fib_Ctrl (F20, F30, EF10), Fib_ATP6 (A1, A2, A3), Cyb_Ctrl (TFSR, 143B+), and Cyb_ATP6 (F06, F07, F08) (at least three biological replicates each, see Fig. S5I). **(E)** ATP content in intact cells in NPC_Ctrl (NI H1, NI H9, NI TFBJ) and NPC_ATP6 (NI A1, NI A2, NI A3) under basal condition and after 4 hours starvation, in Fib_Ctrl (BJ, HFF1, CON1, LR, NFH2), in Fib_ATP6 (A1, A2, A3), in Cyb_Ctrl (TFSR, 143B+), and in Cyb_ATP6 (F06, F07, F08) (at least three biological replicates each, see Fig. S5J-K). **(F)** Resting plasma membrane potential

in NPC_Ctrl (NI H1) and NPC_ATP6 (NI A2, NI A3), each with at least four biological replicates. **(G)** Proliferation curves of NPC_Ctrl (NI H1, NI TFBJ, NI TFC1, NI LR), NPC_ATP6 (NI A1, NI A2, NI A3), Fib_Ctrl (BJ, HFF1, CON1, LR, NFH2), Fib_ATP6 (A1, A2, A3), Cyb_Ctrl (TFSR, 143B+), and Cyb_ATP6 (F06, F07, F08). Cells were kept in either standard medium containing 25 mM glucose (+ glucose) or in medium deprived of glucose containing 10 mM galactose (- glucose, + galactose) (at least two biological replicates each). Error bars represent SD. **(H)** MitoSox fluorescence slope in NPC_Ctrl (NI H1, NI H9, NI TFC1), NPC_ATP6 (NI A1, NI A2, NI A3), Fib_Ctrl (EF1, EF10, EF9, EG1, EM2, FHN409, FHN505, KB2), Fib_ATP6 (A1, A2, A3), Cyb_Ctrl (TFSR, 143B+, EF9R, VFR1), and Cyb_ATP6 (F06, F07, F08) (at least three biological replicates each). In all panels, unless otherwise indicated, error bars represent SEM and p values were determined by unpaired two-tailed Student's t-tests: *P≤0.05, **P≤0.01, ***P≤0.001.

See also Figure S3, Figure S4, and Figure S5.

Figure 5. Mitochondrial hyperpolarization in neural cells carrying the *MT-ATP6* mutation. (A) MMP quantification in permeabilized cells presented as the difference between state 4 respiration (induced by 1 µM oligomycin) and state 3 respiration (induced by 1 mM ADP) (see Fig. S6A-C). At least three biological replicates per line: NPC_Ctrl (NI H1, NI H9, NI TFBJ, NI TFC1), NPC_ATP6 (NI A1, NI A2, NI A3), Fib_Ctrl (F20, F30, EF10), Fib_ATP6 (A1, A2, A3), Cyb_Ctrl (TFSR, 143B+), and Cyb_ATP6 (F06, F07, F08) (see Fig. S5L). **(B)** Imaging-based assessment of MMP in intact cells in NPC_Ctrl (NI H1, NI H9, NI TFBJ, NI TDBJ5, NI O3, NI O6, NI TFC2, NI TDHFF1), NPC_ATP6 (NI A1, NI A2, NI A3), Fib_Ctrl (BJ, HFF1, NFH2, Con1, LR), Fib_ATP6 (A1, A2, A3), Cyb_Ctrl (TFSR, 143B+), and Cyb_ATP6 (F06, F07, F08) (at least three biological replicates each, see Fig. S5M). MMP was calculated by subtracting from the signal of untreated samples the signal obtained after treatment for 30 min with FCCP + antimycin A (both 1 µM). **(C)** Imaging-

based quantification of MMP in intact differentiated Neur_Ctrl (from NI H1, NI TFBJ, NI O6) and Neur_ATP6 (from NI A2 and NI A3) (two biological replicates each, see Fig. S6F). **(D)** High-content screening (HCS)-based quantification of TUJ1-positive cells in Neur_Ctrl (from NI H1, NI TFBJ, NI O6) and Neur_ATP6 (from NI A2 and NI A3) (n=3 for each line). **(E)** Mitochondrial length measured in Neur_Ctrl (from NI TFBJ) and Neur_ATP6 (from NI A3) (at least 60 mitochondria each, out of at least 20 TEM pictures). **(F)** Ultrastructure images of differentiated Neur_Ctrl (from NI TFBJ) and from Neur_ATP6 (from NI A2 and NI A3). Scale bar: 2 µm. In all panels, unless otherwise indicated, error bars represent SEM and p values were determined by unpaired two-tailed Student's t-tests: *P≤0.05, **P≤0.01, ***P≤0.001.

See also Figure S5 and Figure S6.

Figure 6. Altered calcium homeostasis in NPC_ATP6. (A) Hierarchical clustering based on genes regulating mitochondrial calcium homeostasis (see Fig. S6G) in Fib_Ctrl (BJ, HFF1), Fib_ATP6 (A1, A2, A3), PSC_Ctrl (H1, H9, TDHFF1, TDBJ5, TFBJ), PSC_ATP6 (TFA2, TDA2.3, TDA3.1), NPC_Ctrl (NI H1, NI H9, NI TDBJ5, NI TFBJ), and NPC_ATP6 (NI A2, NI A3). **(B)** Expression of three genes involved in mitochondrial calcium homeostasis. p values were determined by ANOVA followed by a Tukey post-hoc test between NPC_Ctrl and NPC_ATP6. **(C)** Global proteomics analyzed as pair-wise comparison between NPC_ATP6 (NI A1, NI A2, and NI A3) and NPC_Ctrl (here shown in comparison to NI TFBJ, similar results were observed with NI H1, NI H9, and NI TFC1). **(D)** Representative images of NPC_Ctrl (line NI TFBJ) and NPC_ATP6 (line NI A3) showing basal cytosolic calcium before stimulation (basal) and at maximal peak Fluo-4 fluorescence after 1 mM glutamate (Glu) stimulation. Scale bar: 50 µm. **(E)** Cytosolic calcium release by exposing permeabilized cells to increasing doses of calcium (a: 5 mM $CaCl_2$, b: 10 mM $CaCl_2$, b: 50 mM $CaCl_2$ in Tyrode's solution). NPC_Ctrl (NI H1, NI TFBJ, NI TDBJ5, NI TFC2; each

with at least three biological replicates) were compared to NPC_ATP6 (NI A1, NI A2, NI A3; each with at least four biological replicates). **(F)** Calcium release from mitochondria in permeabilized cells following exposure to FCCP and antimycin A (both 1 µM). NPC_Ctrl (NI H1, NI TFBJ, NI TDBJ5, NI TFC2; each with at least three biological replicates) were compared to NPC_ATP6 (NI A1, NI A2, NI A3; each with at least four biological replicates). **(G)** Calcium release from the ER in permeabilized cells treated with 1 µM thapsigargin. NPC_Ctrl (NI H1, NI H9, NI TFBJ; each with at least two biological replicates) were compared to NPC_ATP6 (NI A2, NI A3; each with at least three biological replicates). **(H-I)** Calcium responses in permeabilized Cyb_Ctrl (TFSR, 143B+) and Cyb_ATP6 (F06, F07, F08) (at least three biological replicates each). In all panels, unless otherwise indicated, error bars represent SEM and p values were determined by unpaired two-tailed Student's t-tests: *P≤0.05, **P≤0.01, ***P≤0.001.

See also Figure S6, Table S1, and Video S2.

Figure 7. Phenotypic HCS in NPC_ATP6. (A) HCS-based quantification of MMP in live intact cells, using Hoechst for cell determination, TMRE for MMP, and PicoGreen for normalization over mtDNA content. Cellomics ArrayScan was employed according to the "Compartmental Analysis" BioApplication. **(B)** Screening of 130 FDA-approved compounds (all 1 µM in 0.04% DMSO overnight). NPC_ATP6 (NI A2) treated overnight with 0.04% DMSO (dark orange) were used as baseline. Dashed lines refer to 2SD distance from the baseline. Shown here are the average values (two biological replicates, each with two technical duplicates per compound). **(C)** ATP production in permeabilized NPC_ATP6 (NI A1, NI A2, NI A3, two biological replicates each) exposed to either DMSO or 1 µM avanafil overnight (see Fig. S7G). **(D)** ATP content in intact cells in Neur_ATP6 (from NI A2 and NI A3) after overnight treatment with DMSO or 1 µM avanafil (see Fig. S7H). **(E-F)** Cytoplasmic calcium response upon increasing doses of calcium (a: 5 mM $CaCl_2$, b: 10 mM

$CaCl_2$, b: 50 mM $CaCl_2$ in Tyrode's solution) in DMSO-treated NPC_ATP6 (DMSO) (NI A1, NI A2, NI A3; each with at least four biological replicates) and NPC_ATP6 treated with 1 µM avanafil overnight (Ava) (NI A1, NI A2, NI A3; each with at least three biological replicates). **(G-H)** Cytoplasmic calcium response upon FCCP and antimycin A (both 1 µM) stimulation in DMSO-treated NPC_ATP6 (NI A1, NI A2, NI A3; each with at least four biological replicates) and NPC_ATP6 treated with 1 µM avanafil overnight (NI A1, NI A2, NI A3; each with at least three biological replicates). **(I-J)** Cytoplasmic calcium response in permeabilized DMSO-treated Neur_ATP6 (from NI A2 and NI A3) and in the same neurons treated overnight with 1 µM avanafil (see Fig. S7I). **(K)** Left side: suggested mechanisms underlying the impaired mitochondrial calcium handling of NPC_ATP6 cells; right side: potential mode action of avanafil (see discussion for details). CV: Complex V (*MT-ATP6* in orange); H: hydrogen ions (protons); ETC: electron transport chain (Complexes I-IV); MCU: mitochondrial calcium uniporter, NCX: sodium-calcium exchanger; PTP: permeability transition pore; cGMP: cyclic GMP. In all panels, error bars represent SEM and p values were determined by unpaired two-tailed Student's t-tests: *P≤0.05, **P≤0.01, ***P≤0.001.
See also Figure S7 and Table S3.

STAR Methods

CONTACT FOR REAGENT AND RESOURCE SHARING

Further information and requests for reagents may be directed to, and will be fulfilled by, the Lead Contact Alessandro Prigione (alessandro.prigione@mdc-berlin.de).

EXPERIMENTAL MODEL AND SUBJECT DETAILS

Fibroblasts and cybrids

All fibroblast and cybrid cultures were maintained in DMEM medium (Gibco) containing 10% fetal bovine serum (FBS, Gibco), MycoZap antibiotics (Lonza), non-essential

amino acids, Pen/Strep, and sodium pyruvate (all Gibco). The cultures were kept in a humidified atmosphere of 5% CO_2 at 37 °C under atmospheric oxygen conditions.

The patient fibroblasts A1, A2, and A3, all harboring homoplasmic levels of the mutation m.9185T>C in the *MT-ATP6* gene, were previously characterized (Aure et al., 2013). Control fibroblasts included BJ, HFF1 (both from ATCC), Con1, Con2 (both kindly obtained from Dr. Sarah Doss, Charité University), and LR (from Prof. Markus Schülke, Charité University). Ethical approval was obtained by local authorities to use patient fibroblasts for iPSC derivation (IRB code #EA2/131/13) and approval from the State Office of Health and Social Affairs Berlin (LaGeSo) was obtained for the generation of human iPSCs using retroviruses (347/92-25).

Control cybrids and mutant cybrids carrying the m.9185T>C mutation were previously reported (Aure et al., 2013). The mutant cybrids represented three different clones derived from A1 fibroblasts.

Information regarding all individuals and control and patient lines utilized in this study are reported in **Table S5**.

Pluripotent stem cells (PSCs)

hESC lines (H1 and H9) were purchased from WiCell and used according to the German law (personal license to A.P., #AZ: 3.04.02/0077-E01).

Control iPSCs included lines previously generated *via* transduction (TD) of the four Yamanaka retroviral factors, here labeled as TDHFF1, TDBJ4, and TDBJ5, previously reported as iPS2 (Prigione et al., 2010) and iB4 and iB5 (Prigione et al., 2011a), respectively. The retrovirally derived OiPS6 control iPSC line was also previously reported (Prigione et al., 2011b).

All pluripotent stem cells (PSCs) were cultivated on mitotically-inactivated mouse embryonic fibroblasts (MEFs) grown on Matrigel (BD Bioscience)-coated plates, using KO-

DMEM medium (Gibco) containing 20% knock-out serum replacement (KSR, Gibco), 8 ng/µl bFGF (PeproTech), MycoZap antibiotics, non-essential amino acids, Pen/Strep, and sodium pyruvate. For DNA and RNA isolation, PSCs were grown under feeder-free conditions on Matrigel-coated plates using DMEM/F12 medium supplemented with N2, B27, 0.05% BSA (all from Gibco), 8 ng/µl bFGF, and non-essential amino acids, Pen/Strep, and sodium pyruvate. All PSCs were kept in a humidified atmosphere of 5% CO_2 at 37 °C in 5% oxygen conditions.

rNPCs and eNPCs

Rosette-based NPCs (rNPCs) derived from the hESC line H9 were purchased from Aruna (hNP1, Aruna Biomedicals). Brain-derived *ex vivo* adult human NPCs (eNPCs) were bought from Lonza (Normal Human Neural Progenitor Cells, NHNP). All NPC cultures were kept in a humidified atmosphere of 5% CO_2 at 37 °C under atmospheric oxygen conditions.

METHOD DETAILS

Derivation of iPSCs

Control or patient fibroblasts were transduced with four transgene-encoding (OCT4, SOX2, KLF4, and c-MYC) retroviruses to generate transduction (TD)-iPSCs. Alternatively, they were transfected with episomal plasmids (containing the same four factors plus NANOG, LIN28, and SVLT) using Amaxa Cell Line Nucleofector Kit R (Lonza) to generate transfection (TF)-iPSCs. Transfection of episomal plasmids (Yu et al., 2011) was conducted using Amaxa Cell Line Nucleofector Kit R (Lonza), as previously described (Prigione et al., 2014). Pluripotency of the generated lines was confirmed following previously published procedures (Prigione et al., 2010) using both *in vitro* embryoid bodies (EB)-based differentiation and teratoma formation (performed by EPO-GmbH). The karyotype was

assessed by chromosomal analysis after GTG-banding performed at the Human Genetic Center of Berlin, Germany.

Generation of NI NPCs

We obtained neural induction (NI) NPCs following on a previous report (Li et al., 2011) with slight modifications. Briefly, 70% confluent PSCs were split and plated onto feeder-free Matrigel-coated dishes in DMEM/F12 medium. After 24 h, conditions were switched to NI-E medium (Neurobasal:DMEM/F12 [1:1], N2 [1x], B27 [1x], hLIF [10 ng/ml], CHIR99021 [4 µM, Cayman Chemical], SB431542 [3 µM, SelleckChem], Compound E [0.1 µM, Calbiochem], BSA [0.05%], Pen/Strep, and L-glutamine). Medium was changed every other day. After one week, the cells were split as single cells using Accutase (Life Technologies) and further cultured in NI medium (Neurobasal:DMEM/F12 [1:1], N2 [1x], B27 [1x], hLIF [10 ng/ml], CHIR99021 [3 µM], SB431542 [2 µM], BSA [0.05%], Pen/Strep, MycoZap antibiotics, and L-glutamine). NI NPCs were then maintained in NI medium with change every other day. NI NPCs were split at ratios of 1:2 to 1:5 using a cell spatula when confluency reached 80-100%.

Neuronal and astrocyte differentiation

For neuronal differentiation, NI NPCs were plated at different densities (1-3 x10^6 per well) onto surfaces coated with Matrigel, poly-L-ornithine [20 µg/ml], and laminin [5 µg/ml] (both Sigma-Aldrich). For GABAergic neuronal differentiation, NI NPCs were plated on Matrigel, poly-L-ornithine [30 µg/ml], and laminin [5 µg/ml] in GA medium (DMEM/F12, N2 [1x], L-glutamine, Pen/Strep) containing BDNF [20 ng/ml] and SAG [200 nM] (Enzo Life Sciences). After four to five weeks, neuronal-like cells were cultured in GA medium with BDNF [20 ng/ml], IGF [10 ng/ml], and db-cAMP [300 ng/ml]. The maturation phase was extended for several weeks to allow electrophysiological measurements. Generation of

dopaminergic neurons was performed according to a previously published protocol (Reinhardt et al., 2013). NPCs grown on Matrigel were induced to differentiate for 8 days using a medium containing Neurobasal:DMEM/F12 [1:1], N2 [1x], B27 [1x], purmorphamine [1 µM], vitamin C [200 µM], and FGF8 [100 ng/ml] and for 2 additional days using a medium containing Neurobasal:DMEM/F12 [1:1], N2 [1x], B27 [1x], purmorphamine [500 nM], and vitamin C [200 µM]. Cells were then split using Accutase at 1:3 ratios and plated onto matrigel-coated dishes. Conditions were switched to the maturation medium containing Neurobasal:DMEM/F12 [1:1], N2 [1x], B27 [1x], vitamin C [200 µM], db-cAMP [500 µM], BDNF [10 ng/ml], GDNF [10 ng/ml], and TGFbeta3 [1 ng/ml]. Differentiating neurons were kept in these conditions and the medium was changed every other day.

To assess the efficiency of neuronal differentiation from control and patient NPCs, high-content screening (HCS)-based quantification of TUJ1-positive cells was performed. Briefly, NPCs were differentiated into dopaminergic neurons and plated on Matrigel-coated 96-well plates. Cells were grown for 4 weeks (see culture conditions above) and then fixed and stained with TUJ1 antibody and counter-stained with Hoechst (see below for details on staining method). TUJ1-postive cells were counted using the “Neuronal profiling” BioApplication protocol of the HCS microscopy Cellomics ArrayScan (XTI Infinity High Content Platform, Life Technologies).

The differentiation of NI NPCs into astrocytes was promoted by a standardized protocol (Krencik and Zhang, 2011) with slight modifications. In brief, NPCs were cultured as neurospheres in uncoated flasks with NI medium for 3 months during which progenitor clusters switched from neurogenic neurospheres to gliogenic astrospheres. To maintain their size during their expansion, spheres were regularly triturated with a flame-polished Pasteur pipette with smoothened edges and a 0.2-0.5 mm aperture diameter. After 3 months, spheres were dissociated to single cells with enzymatic digestion using Accutase (Life Technologies), transferred to new flasks at a concentration of at least 100,000 cells/ml and allowed to form

new clusters. This process was repeated for a further 30 days. For maturation, dissociated single cells were plated onto acid-etched, poly-L-ornithine - (40 µg/ml) and laminin-coated (40 µg/ml) coverslips at a density of 10,000 cells/cm^2 for 7 days. For this final stage, hLIF, CHIR99021 and SB431542 in NI medium were replaced by rhCNTF (10 ng/ml, PeproTech).

Calcium imaging

Calcium studies were carried out by plating cells on glass bottom microwell dishes (MatTek) and incubating them in Tyrode's solution (in mM: 129 NaCl, 5 KCl, 2 $CaCl_2$, 1 $MgCl_2$, 25 HEPES, 30 Glucose, pH 7.4) supplemented with 5 µM Fluo-4 (Life Technologies) and 0.02% Pluronic F-127 (Sigma) for 45 min at RT and 5% CO_2 in the dark. Fluorescence microscopy was performed using a Zeiss LSM780 confocal microscope system with a 20x objective, using time-series frames with an interval of 2 sec. After baseline interval, stimuli diluted in Tyrode's solution were added, including high KCl (30 mM), L-glutamate (1 mM), FCCP and antimycin A (both 1µM), or thapsigargin (1 µM). Alternatively, increasing doses of calcium (5 mM, 10 mM, 50 mM $CaCl_2$) were added in calcium-free Tyrode's solution (Gandhi et al., 2009). Preincubation with digitonin (0.2 mM) was included for the last three stimuli. For each biological replicate, 10-20 cells were measured. Traces in the graphs represent the normalized average fluorescence intensity change over time. For quantification, the area under the curve (AUC) of the whole Fluo-4 fluorescence peak area was determined using GraphPad Prism.

Whole mtDNA sequence analysis

Total genomic DNA was isolated from cultured cells with the FlexiGene DNA kit (Qiagen). Two overlapping fragments, long 9,932 bp and 9,506 bp, were generated using the Expand Long Template PCR System (Roche). Fragments were separated by electrophoresis on 0.7% agarose gels. Both long fragments were also sequenced using the BigDye v1.3

protocol (Life Technologies) on an ABI3500 genetic analyzer (Applied Biosystems) using oligonucleotides placed at ≈400 bp intervals. Nested sequences were quality tested and aligned at the Cambridge reference sequence using the Geneious v6.0.5 software (Biomatters). Positions that deviated from the reference were annotated by the software and visually inspected.

Global transcriptomics

Total RNA was isolated using the Qiagen isolation kit (Qiagen) and quality-checked by Nanodrop analysis (Nanodrop Technologies, Wilmington, DE, USA). Biotin-labeled cRNA samples were produced and hybridized onto Illumina human-12 BeadChips (Illumina, San Diego, CA, United States). Samples included HFF1, BJ, A1, A2, A3, H1, H9, TDHFF1 (iPS2), TDBJ5 (iB5), TFBJ, TFA2, TDA2.3, TDA3.1, NI H1, NI H9, NI TDBJ5, NI TFBJ, NI A2, NI A3, eNPCs, rNPCs_Ar, and rNPCs_NI. Microarray analysis, PCA plot, and heatmaps were performed using the *R*/Bioconductor packages in the programming language R (version 3.1 or greater). Genes were considered significantly expressed with detection p values ≤ 0.01. Differential expression analysis was performed using the Illumina custom method, using differential p values ≤ 0.01, fold change ratio > 1.5. Pathway analysis was determined by mapping onto KEGG pathways using Database for Annotation, Visualization and Integrated Discovery (DAVID) (http://david.abcc.ncifcrf.gov). We fetched the significance level of normalized expression values corresponding to probe ID using lumi R's (http://bioconductor.org/R package). Variance-stabilizing transformation (VST) was used to deal with sample replicates and robust spline normalization (RSN) for normalization. Significant samples (p-value < 0.05) were further transformed onto log2 scale and their IDs were annotated according to the IlluminaHumanv3.db Bioconductor annotation data package. Expression values of multiple probes for one gene were assigned by their median, resulting in analyzing 34,586 genes for each sample. The list of genes regulating energy metabolism was

based on the Human Glucose Metabolism PCR Array (SA Bioscience, http://www.sabiosciences.com), as previously described (Prigione et al., 2011a).

Microarray raw data for NPCs from different studies were obtained from the National Center for Biotechnology Information Gene Expression Omnibus database under the series accession GSE25673 (Brennand et al., 2011), GSE28595 (Li et al., 2011), GSE40556 (Reinhardt et al., 2013), GSE55107 (Hargus et al., 2014) and GSE57595 (Stein et al., 2014). Datasets were processed and normalized as above. In order to create a matrix of expression level for unique genes in each sample, the datasets were merged by their gene names representing median of their respective probes resulted in a total of 16,493 genes for 198 samples. Differential expression between samples from various datasets was performed by correction of batch effect arising from two different platforms and by normalizing each data set to a sample of the same genotype in order to merge data sets for downstream analysis. The corrected batch effect was confirmed by Principal Component Analysis (PCA). Each gene value was further assigned as their relative abundance value, which corresponded to the expression value of the gene in each sample divided by its mean expression value across the samples. The resulting expression matrix was subjected to hierarchical clustering (Spearman correlation, average linkage) and p-value threshold. Fold change of differential expression between samples on log2 scale was analyzed using linear and Bayesian model algorithms from limma (http://bioconductor.org/R package) and pairwise differential. Heatmaps displaying Z-score were generated with matrix hierarchically clustered. Similar comparative analysis was performed on datasets of different stages of brain development. Brain data was downloaded from Allen Brain Atlas data portal (http://human.brain-map.org/static/download) and a matrix of 17,282 genes and 508 samples was created for further analysis as mentioned above.

Global proteomics

NPC_Ctrl (lines NI H1, HI H9, NI TFBJ, NI TFC1) and NPC_ATP6 (lines NI A1, NI A2, NI A3) were harvested and lysed under denaturing conditions in a buffer containing 4% SDS, 0.1 M DTT, 0.1 M Tris pH 8.0. Lysates were sonicated and boiled at 95°C, each for 5 min. Proteins were precipitated in 100% acetone ON at -20°C and re-dissolved in a buffer containing 6 M GdmCL, 10 mM TCEP, 40 mM CAA, 100 mM Tris pH 8.5. A dilution buffer (10% acetone, 25 mM Tris pH 8.5) in the ratio 1:10 (lysate:buffer) was added. 1% of the total lysates were finally digested by 1 µg trypsin at 37°C, ON. Peptides were acidified with a final concentration of 1% formic acid. 10% of the digest was directly used for LC-MS/MS analysis, the remaining 90% were further fractionated by strong cation exchange (SCX) chromatography with the following 5 SCX buffers: 2, 3, 4, 5 and buffer X, according to (Kulak et al., 2014). Dried fractions were dissolved in 5% acetone, 2% formic acid and subsequently injected for LC-MS/MS analysis. LC-MS/MS was carried out by nanoflow reverse phase liquid chromatography (Dionex Ultimate 3000, Thermo Scientific, Waltham, MA) coupled online to a Q-Exactive Plus Orbitrap mass spectrometer (Thermo Scientific, Waltham, MA). Briefly, the LC separation was performed using a PicoFrit analytical column (75 µm ID × 40 cm long, 15 µm Tip ID (New Objectives, Woburn, MA)) in-house packed with 2.1-µm C18 resin (Reprosil-AQ Pur, Dr. Maisch, Ammerbuch-Entringen, Germany) under controlled temperature of 50°C. Peptides were eluted using a non-linear gradient from 2 to 40% solvent B over 180 min at a flow rate of 266 nL/min (solvent A: 99.9% H_2O, 0.1% formic acid; solvent B: 79.9% acetonitrile, 20% H_2O, 0.1% formic acid). 3kV were applied for nanoelectrospray generation. A cycle of one full FT scan mass spectrum (300−1750 m/z, resolution of 70 000 at m/z 200, AGC target $1e^6$) was followed by 12 data-dependent MS/MS scans (200-2000 m/z, resolution of 35 000, AGC target $5e^5$, isolation window 2 m/z) with normalized collision energy of 25 eV. Target ions already selected for MS/MS were dynamically excluded for 30 s. In addition, only peptide charge states between two to eight were allowed. The label-free software MaxLFQ (Cox et al., 2014), which is integrated into

MaxQuant (version 1.5.0.0) , was used for quantification (Cox and Mann, 2008) and searched against the human proteome database UniProtKB with 88.717 entries, released in 11/2014. A false discovery rate (FDR) of 0.01 for proteins and peptides and a minimum peptide length of 7 amino acids were required. A maximum of two missed cleavages was allowed for the tryptic digest. Cysteine carbamidomethylation was set as fixed modification, while N-terminal acetylation and methionine oxidation were set as variable modifications.

For comprehensive proteome data analysis, we applied gene set enrichment analysis (GSEA, v2.2.1) (Subramanian et al., 2005) in order to see if priori defined sets of proteins show statistically significant, concordant differences between patients and controls. The intensity of detected proteins of each data group was averaged and zero values were replaced by 2 prior to log2 transformation. We used GSEA standard settings, except the minimum size exclusion was set to 10 or 15 and C2 (collection of pathways) or C5 (1454 gene annotations) were used as gene set databases (http://software.broadinstitute.org/gsea/msigdb/index.jsp).

PCR analysis

For long-range mtDNA-PCR, products were generated with nested primers in order to prevent sequencing of the numerous nuclear pseudogenes of the mtDNA (Hazkani-Covo et al., 2010). Both long fragments were sequenced using the BigDye v1.3 protocol (Life Technologies) on an ABI3500 genetic analyzer (Applied Biosystems) using oligonucleotides placed at ≈400 bp intervals, as previously described (Detjen et al., 2007).

Gene expression analysis was performed by quantitative real-time PCR (qPCR) using SYBR Green PCR Master Mix and the ViiA™ 7 Real-Time PCR System (Applied Biosystems). For each target gene, cDNA samples and negative controls were measured in triplicates using 384-Well Optical Reaction Plates (Applied Biosystems). Relative transcript levels of each gene were calculated based on the $2^{-\Delta\Delta CT}$ method. Data were normalized to

the housekeeping genes ACTB and GAPDH and are presented as mean LOG2 ratios in relation to control lines.

For mtDNA copy number, the analysis was carried out with qPCR using LightCycler 480 SYBR Green I Master Mix (Roche) with addition of 10 pM of each primer on a LC480 Roche instrument (Roche) as follows: 95 °C for 10 min, 40 cycles (95 °C for 15 s, 60 °C or 62 °C for 30 s, 72 °C for 30 s), 1 cycle (95 °C for 30 s, 60 °C for 30 s, heating to 95 °C and cooling to 37 °C). mtDNA was quantified as copies per µL by amplification of a fragment of the 12S mtDNA gene, with a standard curve obtained from serial dilutions of the linearized plasmid pGEM®-T Easy (Promega) containing the 12S mtDNA gene. Nuclear DNA was quantified as ng per µL by amplification of the 4401 – 4601 region of the single-copy 28S nuclear gene, with a standard curve obtained from serial dilutions of DNA from control fibroblasts. The mtDNA copy number was then calculated as copies per ng nuclear DNA.

PCR-based restriction fragment length polymorphism (RFLP) analysis with the *MnlI* restriction enzyme of the m.9185T>C mutation was carried out according to a standardized protocol (Aure et al., 2013). Briefly, a 120 bp fragment of mtDNA was amplified from total DNA with Phusion polymerase (NEB) and *MT-ATP6* primers. The product was digested with *MnlI* (NEB; 1 h at 37 °C) and separated in 2.5% agarose gels. Wild type (WT) mtDNA is cleaved by *MnlI* into two fragments of 90 and 30 bp. Similar DNA-based PCR approaches were employed to assess absence of episomal vectors using oriP primers and for fingerprinting of the generated iPSC lines using the primers D21S2055 and DS17S1290, as previously described (Prigione et al., 2010).

The analysis of D-loop polymorphisms was performed as described before (Kirches et al., 2001). Briefly, PCR was performed with a FAM labeled forward-primer and a non-labeled reverse-primer. The products were digested with *HaeIII* and the fluorescent fragment sizes were determined with the ABI3500 Genetic Analyzer using the GeneMarker v1.51 software (SoftGenetics). Signals were transformed into curve diagrams, and the integral below the

curve was taken as the relative amount of the respective length fragment. mtDNA deletions was investigated using two different long-range PCR sets (Deschauer et al., 2004). All primer sequences are reported in **Table S4**.

Immunostaining

Cells were fixed with 4% paraformaldehyde (PFA, Science Services) for 20 min at RT and washed two times with PBS. For permeabilization, cells were incubated with blocking solution containing 10% FBS and 1% Triton X-100 (Sigma-Aldrich) in PBS with 0.05% Tween 20 (Sigma-Aldrich) (PBS-T) for 1 h at RT. Primary antibodies included NESTIN (Millipore, 1:200), PAX6 (BioLegend, 1:200), SOX2 (Santa Cruz, 1:100), TUJ-1 (Sigma-Aldrich, 1:3000), OCT4 (Santa Cruz, 1:300), LIN28 (ProteinTech Europe, 1:300), VIMENTIN (Sigma-Aldrich, 1:300), MAP2 (Synaptic System, 1:100), GFAP (DakoCytomation, 1:20), GABA (Calbiochem, 1:10000), Ki-67 (DakoCytomation, 1:50), NANOG (R&D Systems, 1:200), DACH1 (ProteinTech Europe, 1:100), Smooth Muscle Actin (SMA) (DakoCytomation, 1:200), SOX17 (R&D Systems, 1:50), HES5 (Santa Cruz, 1:50), TH (Millipore, 1:300), and TRA1-81 and SSEA1/3/4 (from Hybridoma Bank, all 1:200). Primary antibodies were diluted in blocking solution and incubated for at least 1 h at RT. Prior to and following the 1 h incubation period with the corresponding secondary antibody (Alexa Fluor, 1:300, Life Technologies), cells were washed once in PBS-T and two times in blocking solution, 5 min each. Counterstaining of nuclei was achieved by incubation with 100 ng/ml 4',6-diamidino-2-phenylindole (DAPI, Vector Laboratories) in PBS for 1 h at RT. All images were acquired using the confocal microscope LSM510 Meta (Zeiss) in combination with the AxioVision V4.6.3.0 software (Zeiss) and further processed with Adobe Photoshop CS-6 (Adobe Systems).

Cell proliferation

PSCs (H1, TFBJ, 8 replicates each) were seeded as single cells at a density of 10,000 cells/well in black-wall, clear-bottom plates (Corning) (coated with Matrigel) in normal StemMACS™ iPS-Brew XF medium (Miltenyi Biotec GmbH, 130-104-368). 10 µM Rock inhibitor (Enzo, ALX-270-333-M005) was added 2 hours before splitting and also after seeding, to promote single-cell survival. Cells were allowed to attach and recover for 72 hours, before changing medium to normal E8 medium (containing 25 mM glucose) or E8-galactose medium (glucose-free, with 10 mM galactose). After the medium change one plate was fixed (day 0). Additional plates were fixed on the following three days at the same time every day.

Other cells (patient and control fibroblasts, NI NPCs, and cybrids) were seeded at a density of 5,000, 20,000 and 40,000 cells/well in black-wall, clear-bottom plates (Corning) (coated with Matrigel for NPCs) in normal DMEM (containing 25 mM glucose) or DMEM-galactose (glucose-free, with 10 mM galactose) for fibroblasts and cybrids and NI medium (containing 25 mM glucose) or NI-galactose (glucose-free, with 10 mM galactose) for NI NPCs. Cells were allowed to attach for one hour, before one plate was fixed (day 0). Additional plates were fixed on the following three days at the same time every day.

For fixation, cells were washed with PBS, incubated for 20 min in 4% PFA and 8.1 µM Hoechst, and washed again with PBS for final storage. The analysis was performed both using fluorescence reading with a Tecan plate reader (Infinite M200) and the count of Hoechst (33342, Invitrogen) -positive spots according to the “spot detector” function of the high-content screening (HCS) analyzer Cellomics ArrayScan (see below). All data were normalized to values obtained at day 0 to obtain a relative proliferation curve.

Bioenergetic assessment

Live assessment of cellular bioenergetics was performed using Seahorse XF24 extracellular flux analyzer (Seahorse Bioscience), as described previously (Pfiffer and

Prigione, 2015). Briefly, 40,000 cells were plated into each Matrigel-coated well of the XF24 well plates and incubated overnight at 37 °C with 5% CO_2. Assays were initiated by removing the growth medium and replacing it with unbuffered media. The cells were incubated at 37 °C for 60 min to allow media temperature and pH to reach equilibrium before starting the simultaneous measurement of mitochondrial respiration (oxygen consumption rate, OCR) and anaerobic glycolysis (extracellular acidification rate, ECAR). After baseline records, four additions (all products at 1 µM and from Sigma) were performed to test mitochondrial respiration functions. First oligomycin, a complex V blocker, inhibited OXPHOS and tested respiration coupling to ATP synthesis. Two consecutive administrations of FCCP, a protonophore uncoupling agent, decreased the MMP, therefore increasing respiration rate, and enabled the quantification of the maximal respiration under maximal mitochondrial uncoupling. The last injection of rotenone, a complex I blocker, and antimycin A, a complex III blocker, caused complete inhibition of mitochondrial respiration, thereby allowing us to probe the non-respiratory oxygen consumption. Normalization to DNA content in each well of the plate was performed using the CyQUANT Kit (Molecular Probes).

Cellular ATP content was determined with the luciferase-based ATPlite Luminescence Assay Kit (Perkin Elmer), according to the provider's instructions (Prigione et al., 2010). Briefly, 7000 cells were seeded in 100 µl medium per well in a 96-well plate and subsequently lysed with 50 µl of a solution that at the same time inactivates the endogenous ATPases. Further addition of 50 µl substrate solution containing Luciferase and Luciferin allows quantification of luminescence occurring upon the reaction with ATP. The emitted light is proportional to the ATP concentration in the cells and was measured with a Tecan plate reader (Infinite M200). Every sample was measured at least in triplicate. Results are presented as picomoles of ATP per 1000 cells.

Extracellular lactate amount was quantified using a Lactate Colorimetric/Fluorometric Assay Kit (BioVision). Briefly, cells were seeded in a 96-well plate at a density of 40,000

cells/well and incubated overnight. The next day, medium was replaced by unbuffered media and incubated for 3 h. Subsequently, the supernatants were collected and lactate measurement was performed according to the manufacturer's instructions. Samples were prepared in triplicates and mixed 1:1 with a reaction mix containing enzymes and a lactate probe to proportionally produce fluorescence that could be measured with a Tecan plate reader (Infinite M200). Normalization by DNA content was accomplished using CyQUANT (Molecular Probes). Results were presented as picomoles of lactate per well per DNA content.

ATP production was carried out as previously described (Aure et al., 2013). Briefly, cells diluted in 1 mM EGTA, 3 mM EDTA, 5 mM K phosphate and 100 mM K MES pH 7.2 were permeabilized with 20 µg digitonin per million cells. Protein concentration was measured before addition of 0.8 % fatty acid free bovine serum albumin. 100 000 cells were incubated with 10 mM pyruvate, 10 mM glutamate, 5 mM malate, 20 mM succinate, 50 µM Ap5A (an adenylate kinase inhibitor), and 1 mM ADP. ATP steady state was then measured at 4 minutes interval (T_0 T_4), followed by addition of 8 µM antimycin A and 1 µM oligomycin and again ATP steady state measurement at 4 minutes interval (T'_0 T'_4). The production of ATP was calculated as $[(T_4 - T_0) - (T'_4 - T'_0)]/(4 \times \text{prot concentration})$ and expressed as nanomoles ATP produced per minute and mg proteins.

Transmission electron microscopy (TEM)

All cells were grown on coated Thermanox plastic coverslips (Nalge Nunc International) and fixed with 2.5% glutaraldehyde in 50 mM sodium cacodylate buffer (pH 7,4) supplemented with 50 mM sodium chloride for at least 30 min at RT. Specimens were washed in the same buffer and post-fixed for 1.5 h in 0.5% osmium tetroxide at RT, followed by 0.1% tannic acid for 30 min and 2% uranyl acetate for 1,5 h. Samples were dehydrated in a graded series of ethanol, embedded in Spurr's resin (Low Viscosity Spurr Kit, Ted Pella, Inc) and polymerised at 60 °C. Ultra-thin sections (70 nm) were prepared using an ultra-

microtome (Reichert Ultracut E, Leica) and mounted on copper TEM grids from. Sections were counter stained with uranyl acetate and lead citrate. Micrographs were recorded at varying nominal magnifications using a Philips CM100 microscope operated at 100 kV, which was equipped with a 1k F114 Fastscan CCD camera (TVIPS) or a Tecnai Spirit microscope operated at 120 kV, which was equipped with a 2k Eagle CCD camera (FEI). For ultrastructural analysis, areas covering entire neuronal cells were imaged automatically on the Tecnai Spirit microscope using the MSI-Raster application within the Leginon system. Regions of interest (up to 50x50 μm^2) were selected at low magnification (560x) and successively imaged at 4400x and 15000x magnification applying a defocus of -100 µm and -4 µm, respectively. Obtained micrographs were then montaged to single images using TrakEM2 within the FIJI software package (Cardona et al., 2012).

MMP quantification in permeabilized cells

Cells were diluted in 1 mM EGTA, 3 mM EDTA, 5 mM K phosphate and 100 mM K MES pH 7.2 and permeabilized with 20 µg digitonin per million cells. Addition of 0.8 % fatty acid free bovine serum albumin and 200 nM rhodamine 123 was followed by distribution of the cells in four bioenergetic conditions: resting basal state= 10 mM glutamate and 5 mM malate, state 3 respiration= 10 mM glutamate, 5 mM malate and 1 mM ADP, state 4 respiration= 10 mM glutamate, 5 mM malate, 1 mM ADP and 1 µM oligomycin, and complete depolarization= 10 mM glutamate, 5 mM malate, 1 mM ADP, 1 µM oligomycin, 8 µM antimycin A and 10 µM CCCP (carbonyl cyanide m-chlorophenyl hydrazone, a protonophore dissipating the inner membrane potential). Fluorescence signal was read on an Accuri C6 flow cytometer after gating the cell population based on forward and size scatters. Mitochondrial membrane potential was then calculated using the Nernst equation and 1% as the volume occupied by mitochondria in the volume of medium illuminated by the laser beam.

Imaging-based MMP assessment in intact cells

Cellomics ArrayScan (XTI Infinity High Content Platform, Life Technologies) was used for automated fluorescence microscopy analysis of MMP. One day prior to the assay, cells were collected by Accutase isolation and seeded on a black-wall, clear-bottom plate coated with Matrigel at a density of 40,000 or 80,000 cells/well on 96-well plates (Falcon) and incubated in NI medium overnight at 37 °C, 5% CO_2. On the day of the assay, live cells were stained for 30 min with 10 nM TMRE (Molecular Probes, Life Technologies) for MMP and 3 µl/ml PicoGreen (Quant-iT™ PicoGreen dsDNA Assay Kit, Life Technologies) for mtDNA content normalization. Control staining was performed in parallel in cells exposed to 1 µM FCCP and 1 µM antimycin A (both from Sigma) to cause complete mitochondrial depolarization. All cells were then washed with PBS and stained with 1:10,000 Hoechst (33342, Invitrogen) diluted in phenol red-free-DMEM for 10 min at RT (or 37 °C). After additional PBS washes, cells were kept in phenol red-free-DMEM for the duration of the assay. Images and analysis of Hoechst, TMRE and PicoGreen stainings were conducted with the Cellomics ArrayScan microscope according to the "Compartmental Analysis" BioApplication. The MMP values were extrapolated from the Cellomics measurements using the formula: TMRE (spot intensity * spot count) / PicoGreen (spot intensity * spot count). The results were calculated for each sample by subtracting the MMP value of the sample treated with FCCP and antimycin A from the MMP value of the sample under untreated conditions. The data are then presented in the paper as (TMRE / PicoGreen, a.u.).

High-content screening (HCS)

For the proof-of-principle compound screening, 130 compounds were taken from a library of 700 FDA-approved drugs (Selleckchem- z65122) **(Table S3)**. The potentiometric TMRE probe signal was normalized to the signal of the fluorescent DNA dye PicoGreen. NI

medium (see supplemental text for details) was supplemented with HEPES (Thermo Fisher) to allow the stable quantification of live MMP in a position-independent manner within 384-well plates. Briefly, 15,000 cells/well were plated on 384-well plates (Falcon) the day before the screening and a final concentration of 1 µM of the compounds was added. The second day, the medium was removed and the cells were stained with 10 nM TMRE and 3 µl/ml of PicoGreen together with 1:50,000 Hoechst diluted in phenol red-free NI medium for 30 min at 37 °C, 5% CO_2. Control staining was performed in parallel with cells exposed to 1 µM FCCP and 1 µM antimycin A (both from Sigma) to induce complete mitochondrial depolarization. After one washing step with NI medium without supplements, cells were kept in phenol red-free NI medium for the duration of the assay.

Each compound was used at a concentration of 1 µM dissolved in 0.04% DMSO and tested in duplicate. The same screening was repeated twice and the values shown in Fig. 7C represent the average of all the replicates. In every HCS plate, the control line NI H1 was included to control for inter-plate variability. Compound-treated and DMSO-treated cells were left overnight in NI medium and assessed for live MMP using 10 nM TMRE and 3 µl/ml of PicoGreen together with 0.2 µg/ml Hoechst (Invitrogen) diluted in phenol red-free NI medium. Treatment with FCCP and antimycin A (both 1 µM, Sigma) was used as positive control. HCS was conducted with Cellomics ArrayScan microscope (Thermo Fisher) and analyzed according to the “Compartmental Analysis” BioApplication.

Mitochondrial reactive oxygen species (ROS) production

The rate of mitochondrial ROS production was measured using the mitochondria-specific probe MitoSOX Red (Life Technologies). After incubation in normal or glucose-free medium for 4 h, cells were harvested in their culture medium, $5x10^5$ cells were loaded with 5 µM MitoSOX Red at 37 °C during 10 min and analyzed by flow cytometry at different time points during 20 min. After gating on cells, the median fluorescence intensity was calculated

for each time point and plotted as a function of time. The relative increase in fluorescence intensity per minute was used to eliminate the bias introduced by different dye accumulation due to MMP variation (Polster et al., 2014).

Electrophysiology

NPCs and neuronal cells were probed on coated coverslips. An EPC-7 amplifier and Patchmaster software (HEKA) were used for patch clamp recordings. Patch pipettes, made from borosilicate glass (Science Products, Hofheim, Germany), had resistances of 3-7 MΩ when filled with the intracellular solution containing (in mM): potassium gluconate (110), KCl (25), NaCl (5), $CaCl_2$ (0.5), $MgCl_2$ (1), EGTA (5) and HEPES (30). The standard extracellular solution (E1) (pH 7.4) contained (in mM): NaCl (140), KCl (5), $MgCl_2$ (1), $CaCl_2$ (2), HEPES-NaOH (10) and glucose (10). Series and input resistances were checked throughout the whole duration of each experiment by applying -5 mV-pulses in the voltage clamp mode at -50 mV.

Resting membrane potential was determined in the current clamp mode at 0 pA. Action potential generation of NPCs and neurons was measured in the current clamp mode by applying a holding current of -5 to -30 pA, so that the membrane potential was -70 mV. Increasing current pulses (300 ms; 5 pA to 50 pA) were applied every 5 sec to evoke action potentials, if any. All patch clamp experiments were performed at room temperature (20–25 °C).

QUANTIFICATION AND STATISTICAL ANALYSIS

Data were expressed as mean and standard deviation (mean ± SD) or standard error of the mean (mean ± SEM) where normality of the distribution could be verified, or as median and quartiles (median [1^{st};4^{th} quartiles]) otherwise. For all experiments, multiple technical

replicates and biological replicates were utilized. Detailed information regarding the number of replicates for each experiment can be found in the respective figure legend.

Significance was assessed using parametric tests (Student's t-test, ANOVA) for normally-distributed data and non-parametric tests (Mann-Whitney U test, Kruskal-Wallis) when normal distribution could not be verified. Data were analyzed using GraphPad-Prism software (Prism 4.0, GraphPad Software, Inc.), Veusz (http://home.gna.org/veusz/), and Microsoft Excel (Microsoft).

DATA AND SOFTWARE AVAILABILITY

Our microarray results have been deposited in the GEO database (accession number GSE70071).

The mass spectrometry proteomics data have been deposited to the ProteomeXchange Consortium (http://proteomecentral.proteomexchange.org) via the PRIDE partner repository (Vizcaino et al., 2013) with the dataset identifier PXD004977.

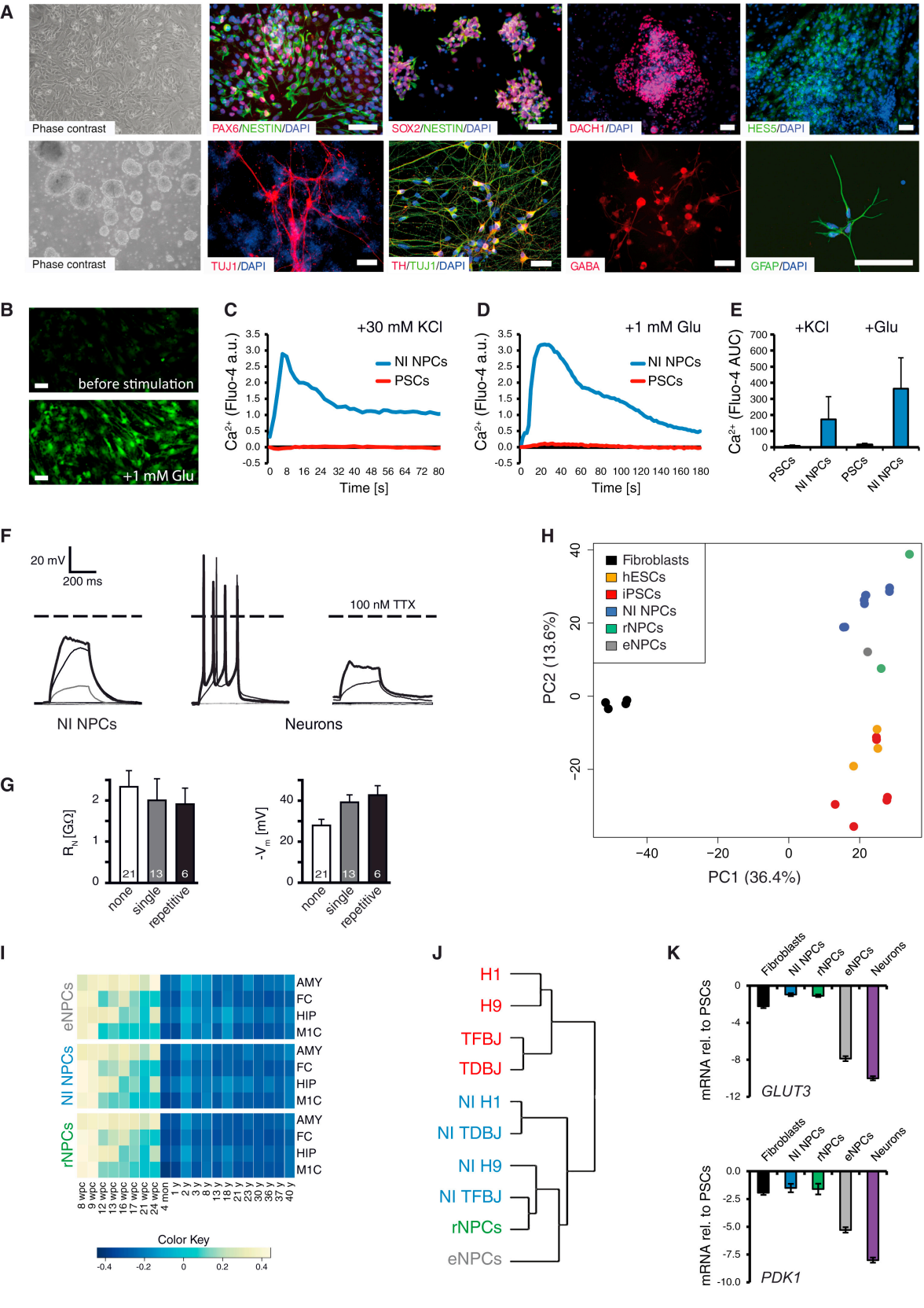
A
Phase contrast
PAX6/NESTIN/DAPI
SOX2/NESTIN/DAPI
DACH1/DAPI
HES5/DAPI
Phase contrast
TUJ1/DAPI
TH/TUJ1/DAPI
GABA
GFAP/DAPI
B
before stimulation
+1 mM Glu
C
+30 mM KCl
NI NPCs
PSCs
Ca2+ (Fluo-4 a.u.)
Time [s]
D
+1 mM Glu
NI NPCs
PSCs
Ca2+ (Fluo-4 a.u.)
Time [s]
E
+KCl
+Glu
Ca2+ (Fluo-4 AUC)
PSCs
NI NPCs
PSCs
NI NPCs
F
20 mV
200 ms
100 nM TTX
NI NPCs
Neurons
G
RN [GΩ]
-Vm [mV]
21
13
6
none
single
repetitive
H
Fibroblasts
hESCs
iPSCs
NI NPCs
rNPCs
eNPCs
PC2 (13.6%)
PC1 (36.4%)
I
eNPCs
NI NPCs
rNPCs
AMY
FC
HIP
M1C
8 wpc
9 wpc
12 wpc
13 wpc
16 wpc
17 wpc
21 wpc
24 wpc
4 mon
1 y
2 y
3 y
8 y
13 y
18 y
21 y
23 y
30 y
36 y
37 y
40 y
Color Key
J
H1
H9
TFBJ
TDBJ
NI H1
NI TDBJ
NI H9
NI TFBJ
rNPCs
eNPCs
K
Fibroblasts
NI NPCs
rNPCs
eNPCs
Neurons
mRNA rel. to PSCs
GLUT3
PDK1

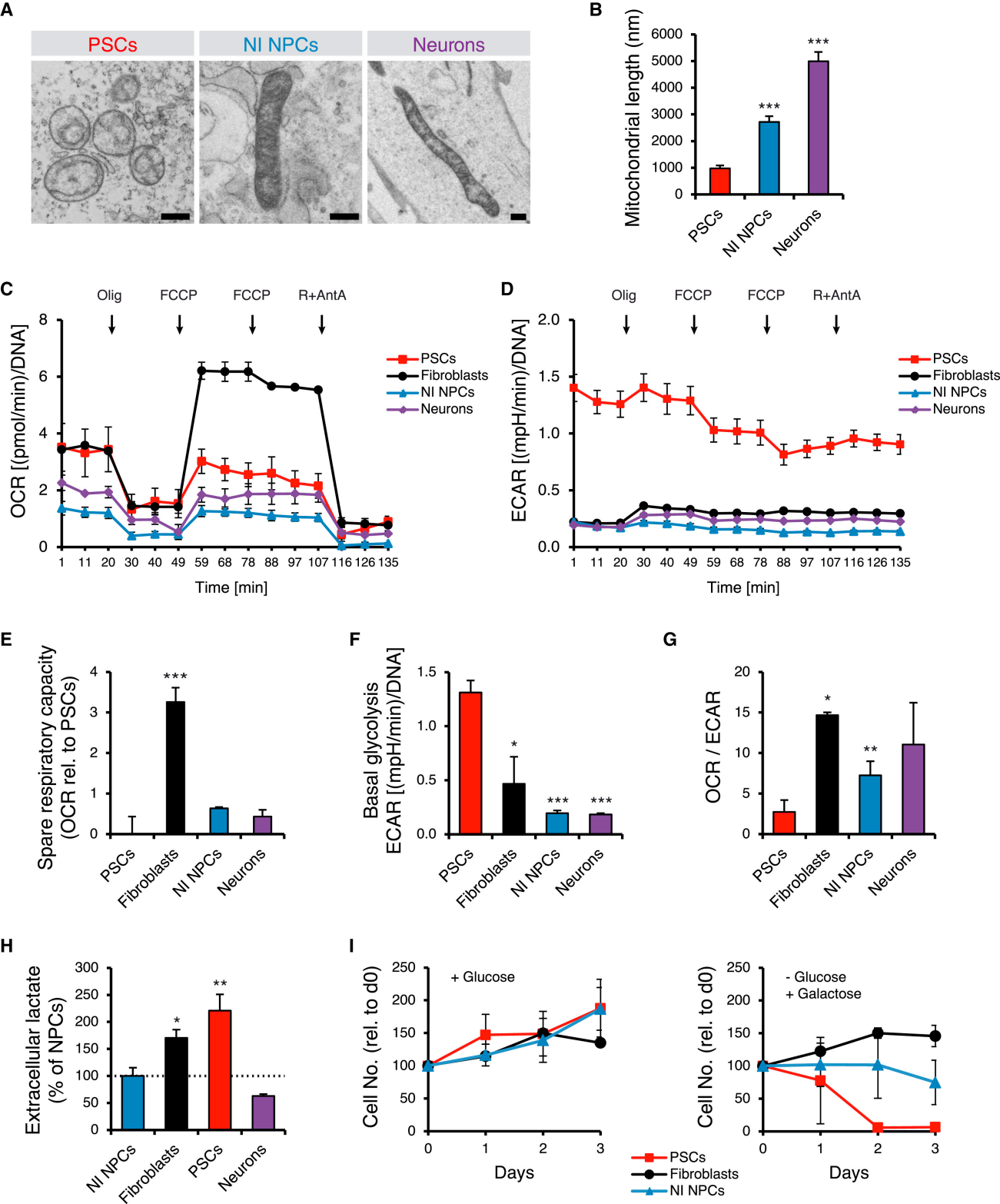
A
PSCs
NI NPCs
Neurons
B
Mitochondrial length (nm)
6000
5000
4000
3000
2000
1000
0
***
***
PSCs
NI NPCs
Neurons
C
Olig
FCCP
FCCP
R+AntA
OCR [(pmol/min)/DNA]
8
6
4
2
0
1 11 20 30 40 49 59 68 78 88 97 107 116 126 135
Time [min]
PSCs
Fibroblasts
NI NPCs
Neurons
D
Olig
FCCP
FCCP
R+AntA
ECAR [(mpH/min)/DNA]
2.0
1.5
1.0
0.5
0.0
1 11 20 30 40 49 59 68 78 88 97 107 116 126 135
Time [min]
PSCs
Fibroblasts
NI NPCs
Neurons
E
Spare respiratory capacity (OCR rel. to PSCs)
4
3
2
1
0
***
PSCs
Fibroblasts
NI NPCs
Neurons
F
Basal glycolysis ECAR [(mpH/min)/DNA]
1.5
1.0
0.5
0.0
*
***
***
PSCs
Fibroblasts
NI NPCs
Neurons
G
OCR / ECAR
20
15
10
5
0
*
**
PSCs
Fibroblasts
NI NPCs
Neurons
H
Extracellular lactate (% of NPCs)
300
250
200
150
100
50
0
*
**
NI NPCs
Fibroblasts
PSCs
Neurons
I
+ Glucose
Cell No. (rel. to d0)
250
200
150
100
50
0
0 1 2 3
Days
- Glucose
+ Galactose
Cell No. (rel. to d0)
250
200
150
100
50
0
0 1 2 3
Days
PSCs
Fibroblasts
NI NPCs

A

Sample	Total variants	Homoplasmic	Heteroplasmic	D-loop	mRNA	tRNA	rRNA
H1	17	14	3	6	6	0	5
NI H1	17	14	3	6	6	0	5
H9	37	36	1	10	20	2	5
NI H9	37	36	1	10	20	2	5
BJ	34	32	2	9	19	1	5
TDBJ4	34	32	2	9	19	1	5
TDBJ5	34	32	2	9	19	1	5
TFBJ.2	34	32	2	9	19	1	5
TFBJ	34	32	2	9	19	1	5
NI TDBJ5	34	32	2	9	19	1	5
NI TFBJ	34	32	2	9	19	1	5

B

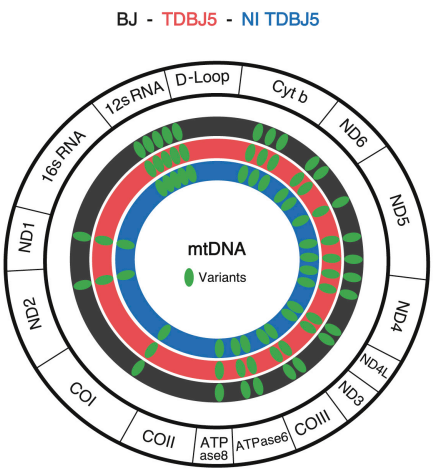

C

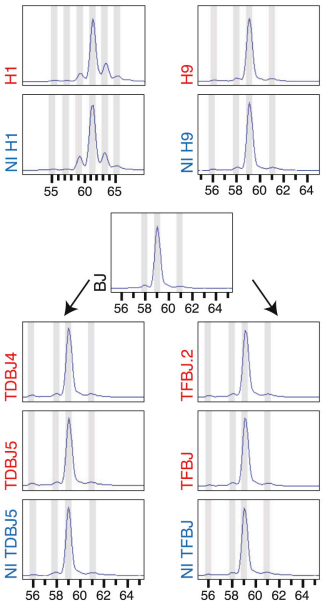

D

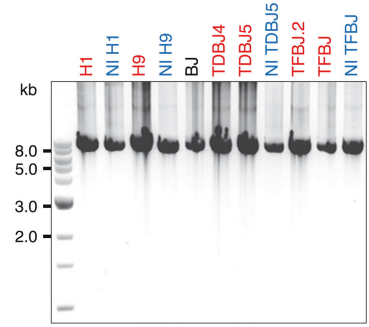

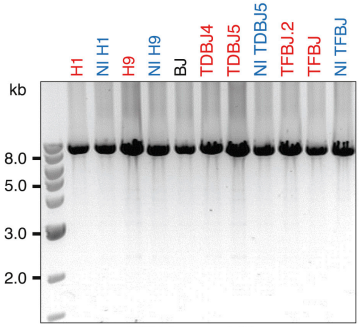

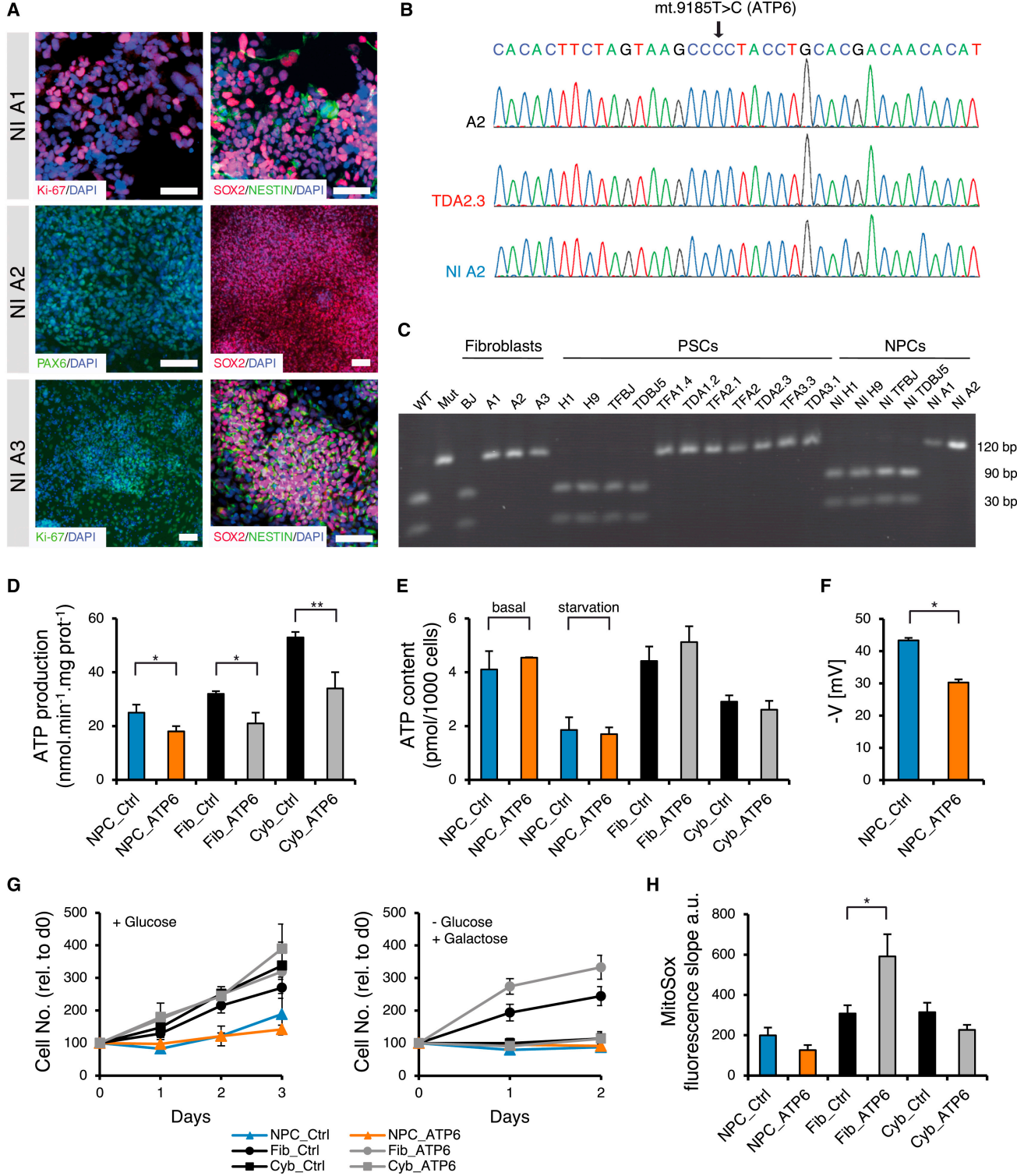
A
NI A1
Ki-67/DAPI
SOX2/NESTIN/DAPI
NI A2
PAX6/DAPI
SOX2/DAPI
NI A3
Ki-67/DAPI
SOX2/NESTIN/DAPI
B
mt.9185T>C (ATP6)
CACACTTCTAGTAAGCCCCTACCTGCACGACAACACAT
A2
TDA2.3
NI A2
C
Fibroblasts
PSCs
NPCs
WT
Mut
BJ
A1
A2
A3
H1
H9
TFBJ
TDBJ5
TFA1.4
TDA1.2
TFA2.1
TFA2
TDA2.3
TFA3.3
TDA3.1
NI H1
NI H9
NI TFBJ
NI TDBJ5
NI A1
NI A2
120 bp
90 bp
30 bp
D
ATP production (nmol.min-1.mg prot-1)
NPC_Ctrl
NPC_ATP6
Fib_Ctrl
Fib_ATP6
Cyb_Ctrl
Cyb_ATP6
E
basal
starvation
ATP content (pmol/1000 cells)
F
-V [mV]
G
+ Glucose
- Glucose
+ Galactose
Cell No. (rel. to d0)
Days
NPC_Ctrl
Fib_Ctrl
Cyb_Ctrl
NPC_ATP6
Fib_ATP6
Cyb_ATP6
H
MitoSox fluorescence slope a.u.

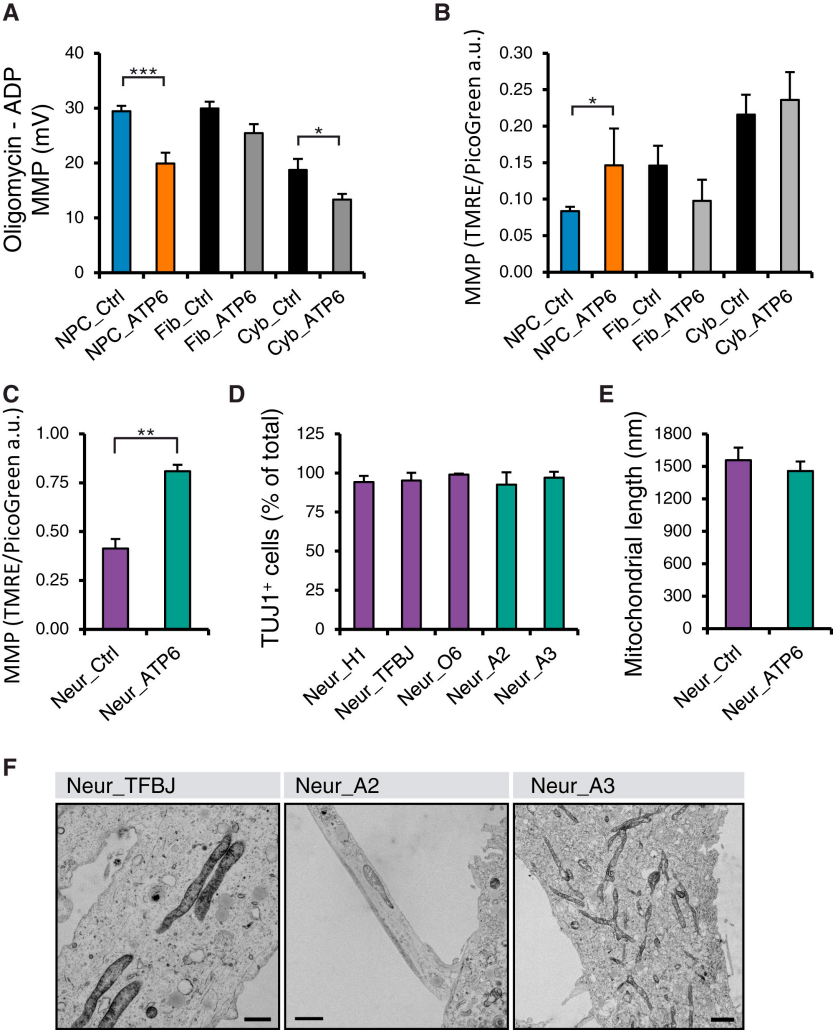
A
Oligomycin - ADP MMP (mV)
40
30
20
10
0
***
*
NPC_Ctrl
NPC_ATP6
Fib_Ctrl
Fib_ATP6
Cyb_Ctrl
Cyb_ATP6
B
MMP (TMRE/PicoGreen a.u.)
0.30
0.25
0.20
0.15
0.10
0.05
0.00
*
NPC_Ctrl
NPC_ATP6
Fib_Ctrl
Fib_ATP6
Cyb_Ctrl
Cyb_ATP6
C
MMP (TMRE/PicoGreen a.u.)
1.00
0.75
0.50
0.25
0.00
**
Neur_Ctrl
Neur_ATP6
D
TUJ1+ cells (% of total)
125
100
75
50
25
0
Neur_H1
Neur_TFBJ
Neur_O6
Neur_A2
Neur_A3
E
Mitochondrial length (nm)
1800
1500
1200
900
600
300
0
Neur_Ctrl
Neur_ATP6
F
Neur_TFBJ
Neur_A2
Neur_A3

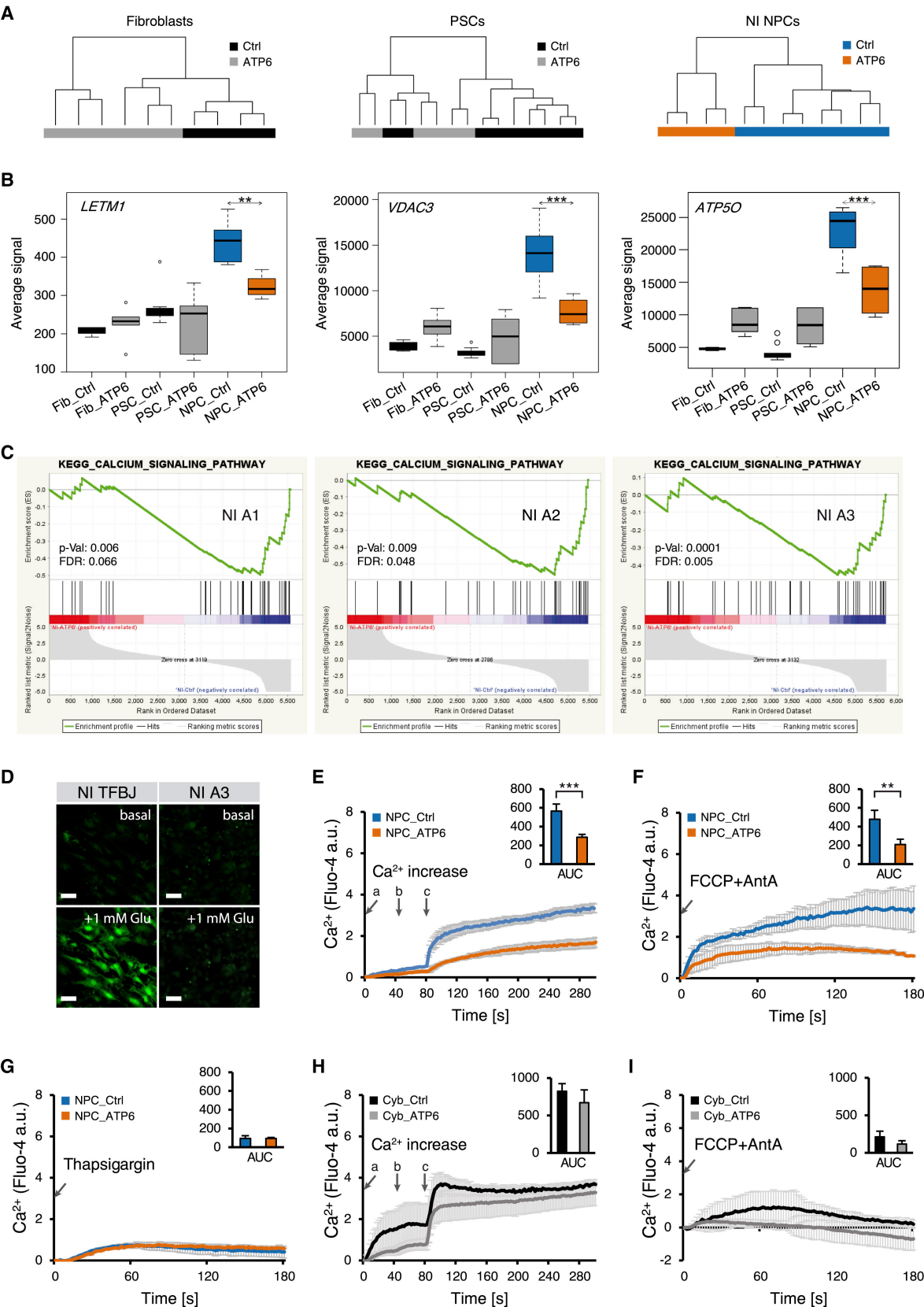
A
Fibroblasts
Ctrl
ATP6
PSCs
Ctrl
ATP6
NI NPCs
Ctrl
ATP6
B
LETM1
**
Average signal
Fib_Ctrl
Fib_ATP6
PSC_Ctrl
PSC_ATP6
NPC_Ctrl
NPC_ATP6
VDAC3
***
Average signal
ATP5O
***
Average signal
C
KEGG_CALCIUM_SIGNALING_PATHWAY
NI A1
p-Val: 0.006
FDR: 0.066
KEGG_CALCIUM_SIGNALING_PATHWAY
NI A2
p-Val: 0.009
FDR: 0.048
KEGG_CALCIUM_SIGNALING_PATHWAY
NI A3
p-Val: 0.0001
FDR: 0.005
Enrichment score (ES)
Ranked list metric (Signal2Noise)
Rank in Ordered Dataset
Enrichment profile
Hits
Ranking metric scores
D
NI TFBJ
NI A3
basal
basal
+1 mM Glu
+1 mM Glu
E
NPC_Ctrl
NPC_ATP6
Ca2+ increase
a
b
c
***
AUC
Ca2+ (Fluo-4 a.u.)
Time [s]
F
NPC_Ctrl
NPC_ATP6
FCCP+AntA
**
AUC
Ca2+ (Fluo-4 a.u.)
Time [s]
G
NPC_Ctrl
NPC_ATP6
Thapsigargin
AUC
Ca2+ (Fluo-4 a.u.)
Time [s]
H
Cyb_Ctrl
Cyb_ATP6
Ca2+ increase
a
b
c
AUC
Ca2+ (Fluo-4 a.u.)
Time [s]
I
Cyb_Ctrl
Cyb_ATP6
FCCP+AntA
AUC
Ca2+ (Fluo-4 a.u.)
Time [s]

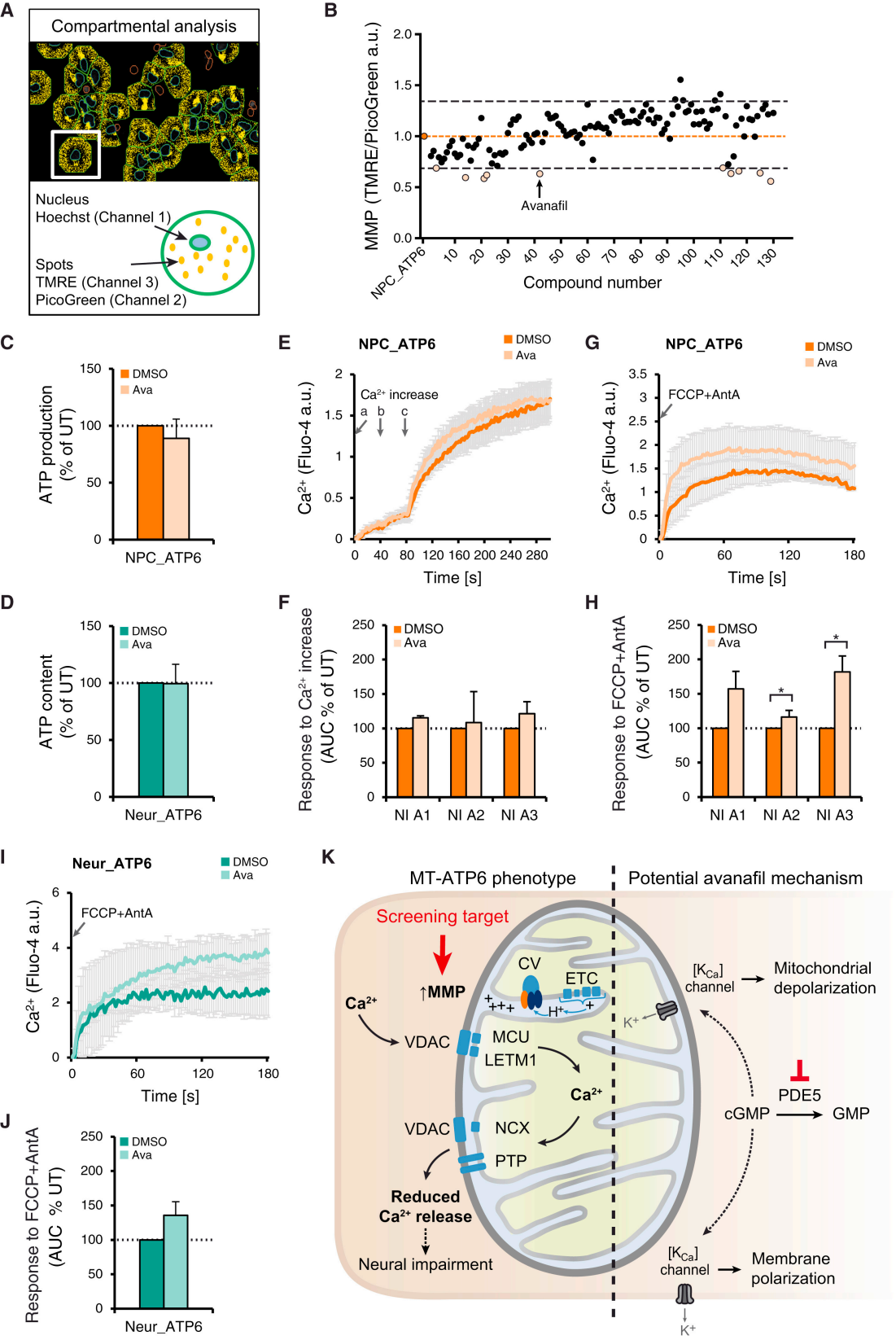
A
Compartmental analysis
Nucleus
Hoechst (Channel 1)
Spots
TMRE (Channel 3)
PicoGreen (Channel 2)
B
MMP (TMRE/PicoGreen a.u.)
Avanafil
NPC_ATP6
Compound number
C
ATP production (% of UT)
DMSO
Ava
NPC_ATP6
D
ATP content (% of UT)
Neur_ATP6
E
NPC_ATP6
Ca2+ increase
a
b
c
Ca2+ (Fluo-4 a.u.)
Time [s]
F
Response to Ca2+ increase (AUC % of UT)
NI A1
NI A2
NI A3
G
NPC_ATP6
FCCP+AntA
H
Response to FCCP+AntA (AUC % of UT)
I
Neur_ATP6
J
K
MT-ATP6 phenotype
Potential avanafil mechanism
Screening target
↑MMP
Ca2+
VDAC
MCU
LETM1
CV
ETC
H+
VDAC
NCX
PTP
Reduced Ca2+ release
Neural impairment
[KCa] channel
Mitochondrial depolarization
K+
PDE5
cGMP
GMP
[KCa] channel
Membrane polarization

KEY RESOURCES TABLE

REAGENT or RESOURCE	SOURCE	IDENTIFIER
Antibodies		
Mouse monoclonal anti-NESTIN, clone 10C2	Millipore	MAB5326
Rabbit polyclonal anti-PAX6	BioLegend	901301
Goat polyclonal anti-SOX2 (Y-17)	Santa Cruz	sc-17320
Mouse monoclonal anti-beta-tubulin (TUJ1), clone 2G10	Sigma-Aldrich	T8578
Mouse monoclonal anti-OCT-3/4 (C-10)	Santa Cruz	sc-5279
Rabbit polyclonal anti-LIN28	ProteinTech Europe	11724
TRA-1-81	Millipore	MAB4381
Mouse monoclonal anti-VIMENTIN, clone V9	Sigma-Aldrich	V6630
Guinea pig polyclonal anti-MAP2	Synaptic Systems	188 004
Rabbit polyclonal anti-GABA	Calbiochem	PC213L
Mouse polyclonal anti-GFAP	DakoCytomation	M076101
Mouse monoclonal anti-Ki-67, clone Ki-67	DakoCytomation	F 0788
Goat polyclonal anti-NANOG	R&D Systems	AF1997
Rabbit polyclonal anti-DACH1	ProteinTech Europe	10914-1-AP
Mouse monoclonal anti-SMA, clone 1A4	DakoCytomation	M0851
Goat polyclonal anti-SOX17	R&D Systems	AF1924
Rabbit polyclonal anti-HES5 (M-104)	Santa Cruz	sc-25395
Rabbit polyclonal anti-tyrosine hydroxylase	Millipore	AB152
SSEA-4	Developmental Studies Hybridoma Bank (DSHB)	MC-813-70
SSEA-3	DSHB	MC-631
SSEA-1	DSHB	MC-480
Biological Samples		
Patient fibroblasts A1, A2, and A3 carrying homoplasmic levels of the mutation m.9185T>C in the *MT-ATP6* gene	Dr. Anne Lombès	Aure et al., 2013
hNP1 Human Neural Progenitor Cells (from WA09)	Aruna Biomedicals	hNP7013.1
Brain-derived *ex vivo* adult human NPCs (eNPCs, Normal Human Neural Progenitor Cells, NHNP)	Lonza	PT-2599
Human ESC line H1	WiCell Research Institute	WA01
Human ESC line H9	WiCell Research Institute	WA09
Mutant cybrids carrying homoplasmic levels of the mutation m.9185T>C in the *MT-ATP6* gene	Dr. Anne Lombès	Aure et al., 2013
Control lines: see Table S5		
Chemicals, Peptides, and Recombinant Proteins		
Matrigel Matrix	BD Biosciences	356231
hLIF	Miltenyi Biotec	130-108-156
CHIR99021	Cayman Chemical	13122
SB431542	SelleckChem	S1067
Compound E	Calbiochem	15579
SAG	Enzo Life Sciences	ALX-270-426-M001
Poly-L-ornithine	Sigma-Aldrich	P4957
Laminin	Sigma-Aldrich	L2020
Thapsigargin	Sigma-Aldrich	T9033
Fluo-4	Life Technologies	F14201
Pluronic F-127	Sigma-Aldrich	P2443
TMRE	Molecular Probes	T669
StemPro Accutase	Life Technologies	A1110501
Recombinant human CNTF	PeproTech	450-13
Rock inhibitor	Enzo Life Sciences	ALX-270-333-M005

FCCP	Sigma-Aldrich	C2920
Antimycin A	Sigma-Aldrich	A8674
Oligomycin	Sigma-Aldrich	75351
Rotenone	Sigma-Aldrich	R8875
N2	Life Technologies	17502048
B27	Life Technologies	17504044
bFGF	PeproTech	100-18B
BDNF	Miltenyi Biotec	130-096-286
db-cAMP	Sigma-Aldrich	D0260-100
Purmorphamine	Miltenyi Biotec	130-104-465
Vitamin C	Sigma-Aldrich	A4403
GDNF	Miltenyi Biotec	130-098-449
TGFbeta3	Miltenyi Biotec	130-094-007
FGF8	R&D Systems	4745-F8-050
BSA	Sigma-Aldrich	A9576
IGF	R&D Systems	291-G1-200
StemMACS iPS-Brew XF	Miltenyi Biotec	130-104-368
HEPES	Sigma-Aldrich	H4034
MycoZap Plus-CL	Lonza	VZA-2012
MitoSOX Red	Life Technologies	M36008
Rhodamine 123	Sigma-Aldrich	R8004
CCCP	Sigma-Aldrich	C2759
HumanHT-12 v4 Expression BeadChips	Illumina	BD-103-0204
Critical Commercial Assays		
Lactate Colorimetric/Fluorometric Assay Kit	BioVision	K607-100
Expand Long Template PCR System	Roche	11 681 834 001
RNA isolation RNeasy Mini Kit	Qiagen	74106
FlexiGene DNA Kit	Qiagen	51206
SYBR Green PCR Master Mix	Applied Biosystems,	4309155
LightCycler 480 SYBR Green I Master Mix	Roche	04707516001
CyQUANT Kit	Molecular Probes	C7026
ATPlite Luminescence Assay Kit	Perkin Elmer	6016941
Quant-iT™ PicoGreen dsDNA Assay Kit	Life Technologies	P7581
FlexiGene DNA kit	Qiagen	51206
Seahorse XF Cell Mito Stress Test	Seahorse Bioscience, Agilent	103015-100
Deposited Data		
Microarray results	GEO database	accession number GSE70071
Mass spectrometry proteomics data	ProteomeXchange Consortium via PRIDE partner repository (Vizcaino et al., 2013)	dataset identifier PXD004977
Recombinant DNA		
Episomal plasmids (OCT4, SOX2, NANOG, KLF4)	Yu et al., 2011	Addgene pEP4 E02S EN2K
Episomal plasmids (OCT4, SOX2, SV40LT, KLF4)	Yu et al., 2011	Addgene pEP4 E02S ET2K
Episomal plasmids (c-MYC, LIN28)	Yu et al., 2011	Addgene pCEP4-M2L
Plasmid pGEM®-T Easy	Promega	A3600
Primers: see Table S4		
Software and Algorithms		

HCS BioApplications (Compartmental analysis, Neuronal profiling)	Cellomics ArrayScan Life Technologies	https://www.thermofisher.com/de/de/home/brands/thermo-scientific/cellomics.html
Geneious v6.0.5 software	Biomatters	https://www.geneious.com/
ViiA™ 7 Software	Applied Biosystems	https://www.thermofisher.com/de/de/home/technical-resources/software-downloads/applied-biosystems-viia-7-real-time-pcr-system.html
GeneMarker v1.51 software	SoftGenetics	http://www.softgenetics.com/GeneMarker.php
AxioVision V4.6.3.0 software	Zeiss	http://www.zeiss.de/mikroskopie/downloads/axiovision-downloads.html
TrakEM2 within the FIJI software package	Cardona et al., 2012	http://imagej.net/TrakEM2
GraphPad Prism Windows 5.04	GraphPad Software, Inc.	http://www.graphpad.com
Database for Annotation, Visualization and Integrated Discovery (DAVID)		http://david.abcc.ncifcrf.gov
R/Bioconductor packages in the programming language R (version 3.1 or greater)		https://www.bioconductor.org/install/
Allen Brain Atlas		http://human.brain-map.org/static/download
MaxQuant (version 1.5.0.0)	Cox and Mann, 2008	http://www.coxdocs.org/doku.php?id=:maxquant:start
Gene set enrichment analysis (GSEA, v2.2.1)	Subramanian et al., 2005	http://software.broadinstitute.org/gsea/index.jsp
Other		
FDA-approved drugs (see Table S3)	Selleckchem	z65122